Montanuniversität Leoben

Investigation on vanadium containing zirconia coatings for high temperature sliding interfaces

Diploma Thesis

by

Oliver Jantschner

This work has been carried out at the Department of Physical Metallurgy and Materials Testing, University of Leoben, Austria, in collaboration with the Air Force Research Laboratory, Materials and Manufacturing Directorate, Wright-Patterson Air Force Base, Dayton, Ohio and with financial support from the European Office for Aerospace Research and Development (EOARD), London, UK.

Affidavit

I declare in lieu of oath, that I wrote this thesis and performed the associated research myself, using only literature cited in this volume.

Leoben, October 30, 2010

Acknowledgment

I would like to thank Univ.-Prof. DI Dr. Helmut Clemens, Head of the Department of Physical Metallurgy and Materials Testing for giving me the opportunity to conduct this work at his department.

Exceptionally I would like to express my gratitude to ao. Univ.-Prof. DI Dr. Christian Mitterer, Head of the Thin Film Group at the Department of Physical Metallurgy and Materials Testing, for assigning this absolutely interesting project to me and all the prolific meetings.

My sincerest gratitude is due to my supervisor DI Dr. Claudia Walter who dampened my youthful enthusiasm so often with persuasive scientific arguments. Thank you for your patience and kindness and your helpful suggestions!

I am very grateful to DI Dr. Rostislav Daniel who showed me that even details have details and that we have to be lucky to be permitted to live with them. Thank's for all the advices and talks!

A special thank to Johannes Pölzl who was my rescuer in all technical problems with "Josephine II".

Many thanks to Mrs. Hilde Stopar for all the unbureaucratic accommodations during my work at the department.

Furthermore thanks to DI Stephan Grasser who showed me the beauty of LaTeX.

I'm much obliged to DI Dr. Robert Franz and Dr. Ronald Bakker for the Laser Raman Microprobe investigations, DI Sophie Primig for the helping hand during DSC measurements, Silvia Pölzl for the assistance after the explosion and DI Dr. Kerstin Chladil and Siegfried Schider for Nanofocus analysis.

It can't be taken for granted that everybody of the thin film group is so amiable and cooperative all the time. Thank you for the coffee breaks, it's great fun to work with you!

Last but not least..... danke ich meiner Familie, meiner Freundin Marlene und meinen Freunden für deren Unterstützung insbesondere während der Diplomarbeit.

Contents

1 Introduction

If a new material has to be developed or an already existing one is to be applied it is important to know what ambiance conditions for. The surface near region which is permanently exposed to the environment has become one of the most important parts of materials engineering. At the interface between material surface and environment numerous energetic exchange processes take place. Every surface has to withstand various outer influences which can be physical or chemical in nature. Therefore, improving the surface of an object by application of a coating can in many cases significantly improve its overall performance. In the last decades numerous coating deposition processes were developed to improve material performance and adapt the surface to the specific environment it has to function in. This investigation focuses on coatings for high temperature sliding interfaces.

1.1 Coating Design Concept

In the realm of modern thin film technology a new type of nano-structured coatings, so called “chameleon coatings”, was established in recent years. They show multifunctional properties to respond to changing environmental conditions like the skin of a chameleon which changes its color according to requirements. This can be realized by controlled reversible surface reactions and/or phase transformations. The concept of chameleon coatings which is shown in Fig. 1.1 was introduced by Voevodin and co-workers combining different solid lubricants into a yttrium stabilized zirconia (YSZ) matrix which provides good mechanical properties and high thermal stability. Solid lubricants such as MoS_2 and WS_2 as well as DLC (diamond like carbon) have already successfully been tested for a temperature range up to 500 °C and changing environments. A hard nanocrystalline phase like YSZ provides good mechanical performance whereas the nanocrystalline or amorphous MoS_2 and DLC inclusions are used to achieve adjustment of transfer films in the friction contacts [1]. These inclusions change their chemical and structural behavior in high/low temperature cycle tests under dry/humid environmental conditions reversibly. However, the common solid lubricants, such as graphite, molybdenum disulphide and polytetrafluoroethylene (PTFE) are effective from low temperatures up to 200-400 °C in air. Above 400 °C they lose their lubricious nature because of oxidation and decomposition [2]. Above 500 °C other lubrication effects take place like diffusion of soft metals from the coating to the surface near region followed by crystallization. This leads to easy shearing transfer films and to high temperature lubrication with friction coefficients of about 0.2 [3]. Ag, Au, ReO, and V_2O_5 are promising solid lubricants for an intermediate temperature range above 500 °C [4].

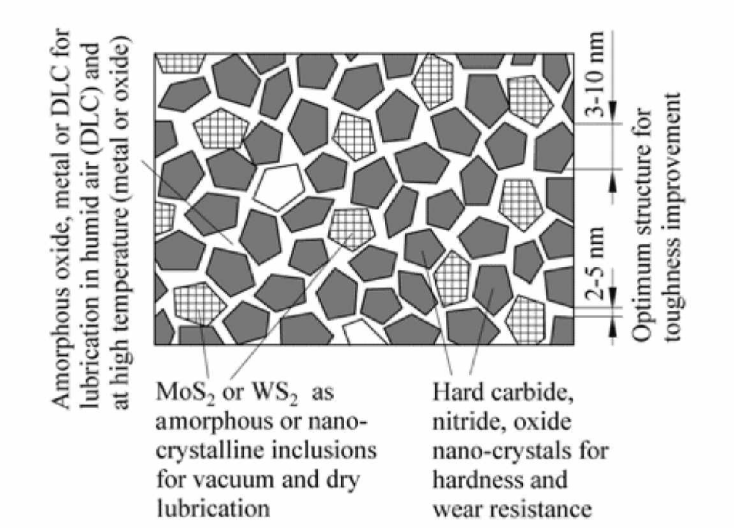

Fig. 1.1: Coating design concept by Voevodin and co-workers adapted from [1].

In this work the influence of varying contents of V_2O_5 on nanostructured zirconia thin films was investigated with respect to their self-lubricious properties and thermal management abilities for high temperature sliding interfaces. The aim is to examine if there is a dispersion or solid solution of V_2O_5 in the zirconia matrix that is able to form a lubricious film on the surface close to its melting temperature. This would create coatings that show beneficial tribological properties with low friction and wear over an extended temperature range. Furthermore, the aim of this work is to show if there is any (endothermic) melting process of the V_2O_5 to absorb local flash temperatures, for example in case of friction in highly loaded sliding contacts.

The general coating design is targeting incorporation of V_2O_5 into a ZrO_2 matrix. The ZrO_2 matrix provides good mechanical properties and high thermal stability against oxidation whereas V_2O_5 shall improve the sliding properties and consume energy to decrease local temperature peaks when melting.

1.1.1 ZrO_2

ZrO_2 also known as zirconia, is one of the most investigated ceramic materials. Its hardness is denoted as 19 GPa and its Young's modulus as 210-231 GPa for thin films [5]. ZrO_2 exists in three different phases: The monoclinic phase (Baddeleyite) (Fig. 1.2) which is stable at room temperature and transforms into the tetragonal phase at 1000-1200 °C. It's unit cell dimensions are $a = 5.169$, $b = 5.232$, $c = 5.341(\pm 0.008)$ Å and $\beta = 99°15'(\pm 10')$. "The structure of Baddeleyite is an interesting combination of fluorite-like layers parallel to (100) in which the oxide ions are tetrahedrally coordinated, with layers in which the oxide ions are in triangular coordination" [6]. The tetragonal phase is stable up to 2350 °C where the phase transformation tetragonal $\leftrightarrow$ cubic takes place. Over 2350 °C the cubic phase occurs up to the melting point at 2715 °C [7]. For high temperature resisting materials phase transformations generally have to be excluded because of volume switches and changing chemical potentials. The ZrO_2 can be stabilized with Y_2O_3 to avoid phase transformations in the temperature range from room temperature (RT) up to 2000 °C which is called yttrium stabilized zirconia (YSZ). The coatings prepared for this thesis are non-stabilized zirconia coatings because of a planned operation and testing range up to 800 °C where no phase transformations are expected.

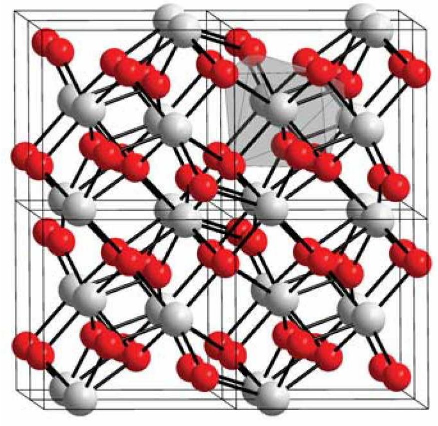

Fig. 1.2: Unit cell structure of monoclinic ZrO_2 (Baddeleyite) stable at RT adapted from [8].

1.1.2 V_2O_5

The binary system V-O includes a multitude of different phases where V has a mean valence between 0 e.g. in $VO_{0.3}$, and +5 e.g. in V_2O_5. The complexity of the V-O system is visualized in Fig. 1.3 which shows the triclinic Magnèli series V_nO_{2n-1} and V_nO_{3n-1}

between 60 and 72 at% oxygen formed in a congruent reaction. Very important for this work is the orthorhombic V_2O_5 at about 71 at% oxygen in the series V_nO_{3n-1} with a melting point of 665 °C. The melting point of VO_2 which is stable at high temperatures is designated at 1957 °C.

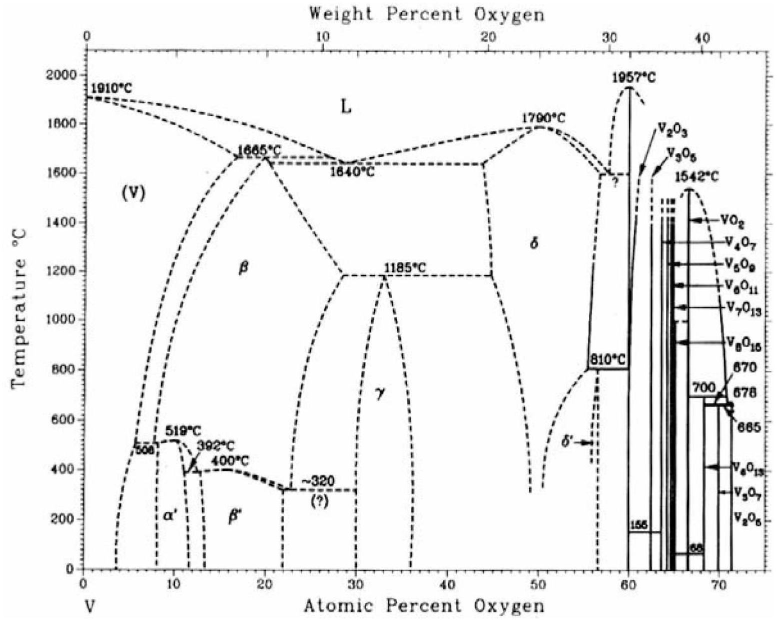

Fig. 1.3: V-O binary phase diagram adapted from [7].

V_2O_5 has low hardness (3.2 GPa) and Young's modulus (79.4 GPa) values compared to ZrO_2 [9]. Its single layer structure is schematically shown in Fig. 1.4. It corresponds to the V_nO_{2n+1} series where n=2,3,6 with fcc structure. There are some polymorphs of V_2O_5 like α-V_2O_5 (orthorhombic), β-V_2O_5 (monoclinic or tetragonal) and δ-V_2O_5 (a modification of β-V_nO_{2n+1}) [10]. The most stable phase is the orthorhombic one. It is the most important vanadium compound because it reversibly loses oxygen upon heating [11] and is so a useful catalyst for several oxidation reactions.

During annealing of V_2O_5 films in vacuum atmosphere at 400-600 °C a reduction to VO_2 which follows the sequence $V_2O_5 \longrightarrow V_3O_7 \longrightarrow V_4O_9 \longrightarrow V_6O_{13} \longrightarrow VO_2$ occurs [13]. The tribological behavior of V_2O_5 single layer coatings and VN-V_2O_5 bi-layer coatings has already been investigated in a temperature range between 25 and 500 °C. It has been demonstrated that these coatings have decreasing friction coefficients at higher temperatures because of thermally activated easy shearing lattice planes [14]. Vanadium oxides following the sequence V_nO_{2n+1} belong to the family of Magnèli phases. They show a high concentration of vacancies and different stoichiometries which leads to reduced binding strength. Furthermore, for some metal oxides shown in Fig. 1.5

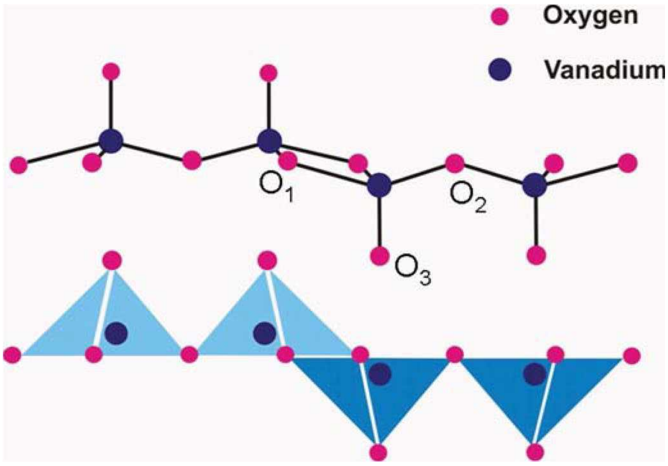

Fig. 1.4: Single layer structure of V_2O_5 adapted from [12].

there is a correlation between ionic potential and friction performance. At 700 °C a thin molten and thus lubricious V_2O_5 layer on the surface provided friction values as low as 0.2. Further friction coefficients already measured are 0.8 at 100 °C, 0.4 at 400 °C and 0.3 above 400 °C. For the suggested coating design concept V_2O_5 is expected to be incorporated as dispersion in the zirconia matrix to obtain partial melting of the coating.

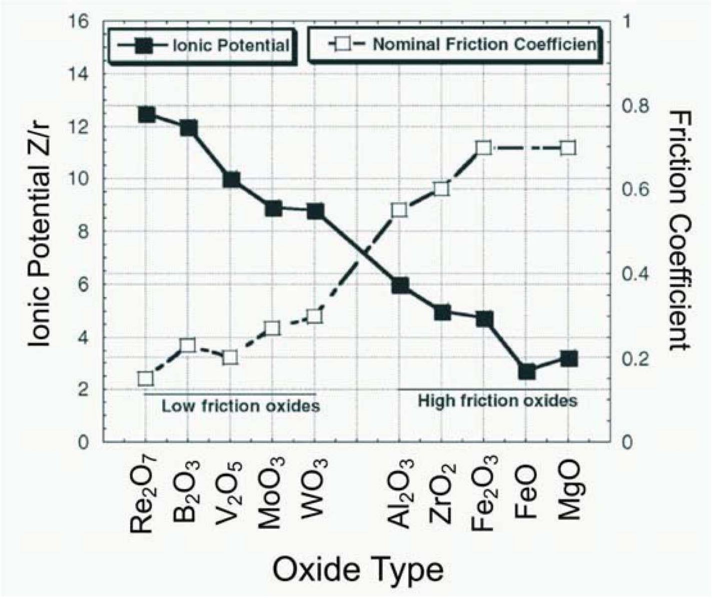

Fig. 1.5: Correlation between ionic potential and friction behavior of some metal oxides [15].

2 Sputter Deposition

The technique of sputtering is an important sub discipline of physical vapor deposition (PVD) processes. These are vacuum based deposition methods for preparing metallic or non metallic thin films for various applications.

PVD in general means three steps of material transport:

1. Transition of a liquid or solid phase into a vapor
2. Transport of the vapor to the substrate
3. Condensation of the vapor at the substrate surface followed by nucleation and growth.

PVD processes can be classified by the mechanisms of vapor generation: a) evaporation of the source material due to heating upon its boiling point at evacuated atmosphere and b) sputtering which means the vapor generation of a material due to momentum transfer processes at its surface which is caused by ion bombardment (mostly ions from a noble gas e.g. Ar^+ ions) (Fig. 2.1). One of the main advantages of PVD is that the depositions can be run at relatively low temperatures in a range of 100-500 °C. Coatings synthesized with PVD techniques are mostly far away from their thermodynamical equilibrium [14]; this means that they can form metastable structures which are responsible for their special mechanical or thermal behavior [16, 17].

2.1 Sputter Mechanisms

"Sputtering is the material erosion tool" on atomic scale [19]. It could remind someone of sandblasting. Instead of sand the "working" particles are ions of noble gases (working gas) to avoid reaction with the sputtered material. The energetic ions provided by a glow discharge (plasma) and accelerated by an electric field eject atoms out of the target surface. The Ar^+ ion becomes neutral because of Auger neutralization before impact [17]. These processes take place in evacuated atmosphere with controlled gas flows to

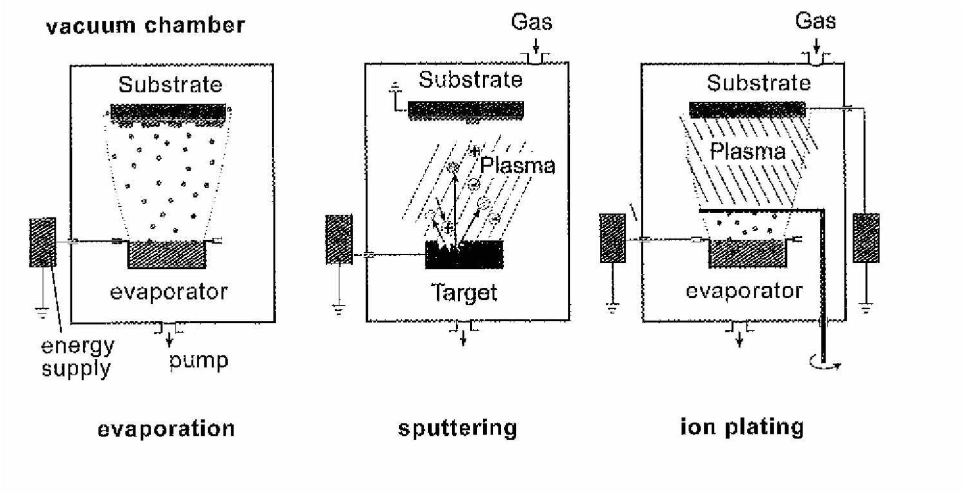

Fig. 2.1: Three types of PVD processes [18].

achieve vaporisation and/or reaction of the ejected atoms to synthesize favored material compositions (reactive sputtering). Ionization of argon leads to a gaseous medium which contains charged (electrons, ions, charged molecules) and neutral (atoms, molecules) particles with general collective behavior, a plasma. Because of local concentrations of positive and negative particles a relative motion of ions occurs. This can be amplified by an outer electric field whereby the charged particles are accelerated and gain kinetic energy. When these energetic particles impinge on a material surface, the ion loses its energy to the target through a series of collisions (collision cascade). If their kinetic energy exceeds the atom bonding energy an atom or molecule may be emitted [16, 17].

2.2 Nonreactive Magnetron Sputtering

The effectiveness of the sputtering process depends on the energy amount of Ar^+ ions present. The main ionization reaction can be indicated as $e^- + Ar \rightarrow e^- + Ar^+ + e^-$. To achieve sufficient sputter rates it has to be assured that enough electrons are near the target surface which increase the probability of ionization of the working gas. This is achieved by placing an array of permanent magnets behind the target which is called a magnetron. A cylindrical magnetron as used in this diploma thesis is shown in Fig. 2.2. In case of diode sputtering the mean free path of the electrons is very long, so they gain much kinetic energy on the way to the anode but do not produce enough ions needed for effective sputtering. When a planar circular magnetron is used, the electrons are kept close to the target surface region for longer producing more ions. In magnetrons a magnetic field parallel to the target surface is produced. The electrons are accelerated perpendicular to the field lines in direction to the target surface. The negative voltage accelerates secondary electrons which result from the ionization procedures and ion bombardment. Under the Lorentz force $\vec{F} = e * (\vec{v} \times \vec{B})$ (where $\vec{B}$ is the magnetic field, e the charge of the electron and $\vec{v}$ the velocity of the electron) of the magnetic field the electrons are operated in semicircular orbits when accelerated away due to a negative potential. This increases their retention time close to the target surface and the chance of an ionizing collision with an argon atom. $\vec{F}$ is proportional to the electron energy. Magnetrons can be classified with respect to their geometries which are important for the formation of the magnetic field lines. For this work only planar circular magnetron arrangements were used in unbalanced mode. That means that the magnetic flux from one pole is unequal to the other. The outer magnetron ring for example has more magnetic material than the inner pole. Unbalanced magnetrons let more electrons escape from the target surface and so increase ion and electron bombardment of the growing film [17].

2.3 Reactive Magnetron Sputtering

Reactive magnetron sputtering is often used to deposit oxide or nitride coatings. For this technique metallic target materials are sputtered in the presence of a reactive gas, e.g. O_2 or N_2. This can be preferable to sputtering oxide or nitride targets directly because oxides and nitrides have ionic and/or covalent bond shares and high binding energies compared to metals. Much more energy is needed to knock out atoms or molecules. This

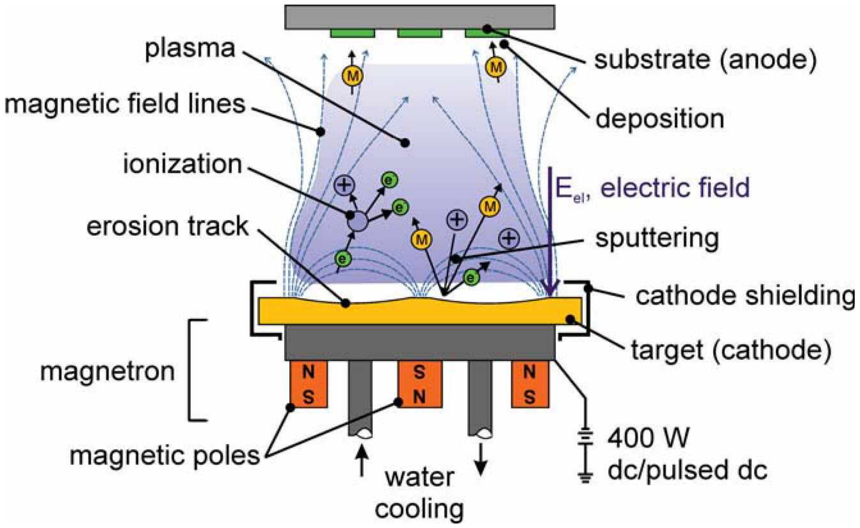

Fig. 2.2: Particle interactions of unbalanced magnetron sputtering [20].

leads to lower sputter yields and increased deposition times. In this diploma thesis, the atmosphere in the deposition chamber consists of Ar and O_2 plasma. The oxygen reacts with the sputtered Zr and V to form the respective oxides in the coating.

Beyond reaction of the O_2 with the sputtered metal ions, an oxidation reaction already happens on the target surface which is called target poisoning. Target poisoning causes a significant decrease of the sputter rate as well as the formation of material compounds on the target surface. For the vanadium oxygen system which is important for this work, depending on the partial pressure of O_2 a large number of possible phases can be formed which occupy the target surface. This increases the complexity of the sputtering process and has to be taken into account when analyzing the composition and structure of the resulting coating [17, 21, 22].

3 Experimental Details

3.1 Coating Deposition

3.1.1 Deposition System

All coatings for this work were deposited by a DC reactive unbalanced magnetron sputtering device at the Montanuniversität Leoben, as schematically shown in Fig. 3.1.

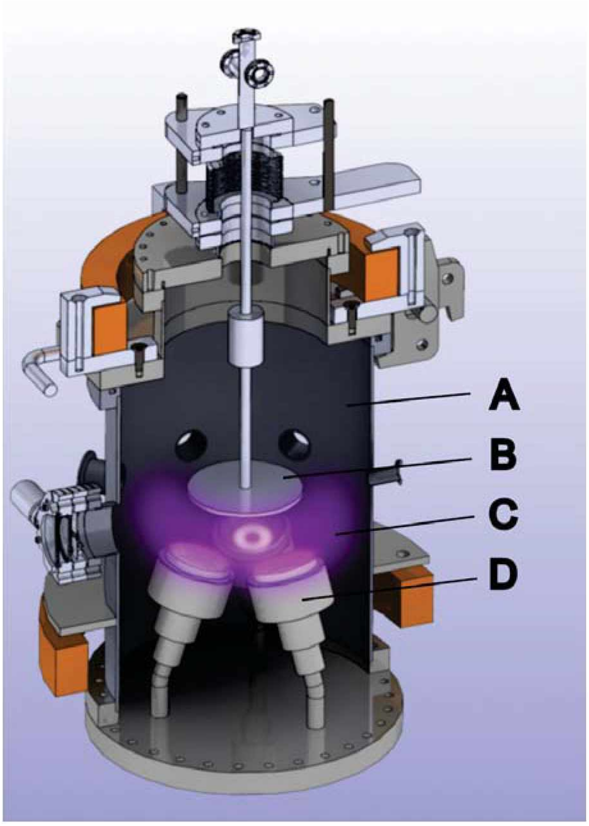

Fig. 3.1: Schematic of the reactive unbalanced magnetron sputtering device used in this work showing the stainless steel chamber (A), the rotatable substrate holder (B), the plasma burning between substrate holder and magnetrons (C) and three cathodes (D).

The sputtering system consists of a cylindrical stainless steel chamber (⌀ 380 × 235 mm) (A) which houses a horizontal circular magnetron cluster with three water-cooled magnetrons (D). The magnetrons are radial swivel-mounted up to 18° inclined from their vertical position. Three metallic 2" targets which are protected with air pressure controlled shutters are fixed on the magnetrons. The rotatable substrate holder (B) which is arranged equiplanar beyond the magnetron cluster in a distance of $\approx$ 75 mm can be heated up to 800 °C. The Ar plasma (C) burns between the magnetron cluster and the rotatable substrate holder. Two MKS ENI RPG-50 (programmable frequency 50-250 kHz, duty cycle from 0.5 µs - 40 %) pulsed DC generators are used for the magnetron power supplies. Two targets (for this work two metallic Zr targets) are supplied by one generator in parallel circuit way. The second generator supplies the third target (for this work a metallic V-target). A third MKS ENI RPG-50 generator is used for plasma etching of the substrates by applying a negative bias voltage. For vacuum generation in the deposition chamber a dual stage rotary vane pump (Pfeiffer Vacuum Duo 20, pumping speed 24 m^3/h N_2) and a turbomolecular pump (Pfeiffer Vacuum TMH 521 P, pumping speed 300 l/s N_2) are used.

3.1.2 Deposition Procedure

All coatings were deposited on three different substrates: AISI M2 high speed steel, Si (100) wafers, and Fe-foil. M2 substrates which were quenched and tempered to a hardness of 65 HRC and afterwards polished were used to conduct tribological tests. A further set of depositions was done on Si wafers for measuring the stress behavior of the coatings on a well known substrate. For the DSC measurements the coatings were synthesized on Fe-foils to make a powder of the coating by dissolution of the foil in 15 % HNO_3. The deposition procedures are shown in Table 3.1. All substrates were ultrasonically cleaned in acetone and ethanol for 10 min and afterwards dried by a hot air gun. The substrates were fixed on the substrate holder (B) which was mounted in the deposition chamber (A). For further substrate cleaning all substrates were plasma etched for 5 min at a temperature of 300 °C after evacuation down to a total pressure of at least 1×10^{-5} mbar. Plasma was ignited between the substrate holder and the magnetrons using a high gas flow of 200 sccm Ar (99.9 % purity) which lead to a total pressure increase up to 10^{-3} mbar and by applying a negative bias voltage of -300 V to force collisions of the Ar^+ ions at the substrate surface. Afterwards the heater was adjusted to a deposition substrate temperature of 150 °C which was kept constant for all coating syntheses. The Ar gas flow was turned off and evacuation down to a pressure below 5×10^{-6} mbar was conducted again. The ratio of the gas flows of Ar (working gas) and O_2 (reactive gas) was also kept constant at 30:10 sccm during all depositions for this work. Constant gas flows and substrate temperature allow an easy comparability of the effects of different target currents and V-contents of the coating. The current density on each Zr-target was kept constant at 17.8 mA/cm^2. The substrate holder was rotating all the time at maximum speed of 20 rpm. The deposition times were varied so that all coating thicknesses were higher than 1 µm.

Tab. 3.1: Deposition runs with varying parameters.

Current density on V-Target [mA/cm^2]	Deposition [min]	Substrate
0	240	M2
0	240	Si
4.1	360	M2
4.1	240	Si
4.1	400	Fe-Foil
7.6	240	M2
7.6	240	Si
7.6	240	Fe-Foil
17.8	240	M2
17.8	240	Si
17.8	260	Fe-Foil

3.2 Coating Characterization

3.2.1 Coating Thickness Measurement

The measurements were carried out by the "ball crater technique" [23] which is schematically shown in Fig. 3.2. It is a very common method because of its quick and easy applicability and quite good accuracy of 2-5 % for coating thicknesses in the range of 0.3-10 µm [24].

A circular wear track in form of a ball scraper is grinded by a rotating steel ball with a diameter D of $\oslash$25.4 mm which is moistened with a diamond suspension. Measuring the inner diameter D_i which is the boundary of the substrate and the coating and the outer diameter D_0 by an optical light microscope the film thickness t_c can be evaluated

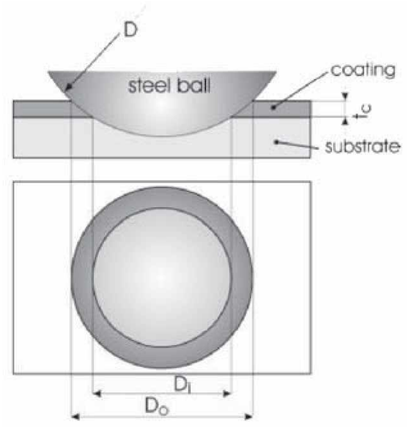

Fig. 3.2: Schematic of the ball crater technique.

by

$$t_c \cong \frac{D_0^2 - D_i^2}{4D}. \tag{3.1}$$

The grinding parameters like spin speed and contact pressure as well as grinding time were varied in such a way that the outer diameter D_0 was in the range of 1 mm. Both diameters could easily be measured.

3.2.2 Coating Adhesion Measurement

A Rockwell-C indentation test (DIN 50103 Part1) gives a good first estimate of coating adhesion at RT. After indentation the indents were examined with the white light microscope in a purely qualitative way by comparing with a predetermined adhesion table after VDI guideline 3824 (shown in Fig. 3.3). HF 1 shows the best adherence with a fine crack network around the indent but no delamination. HF 5 and HF 6 show no suitable

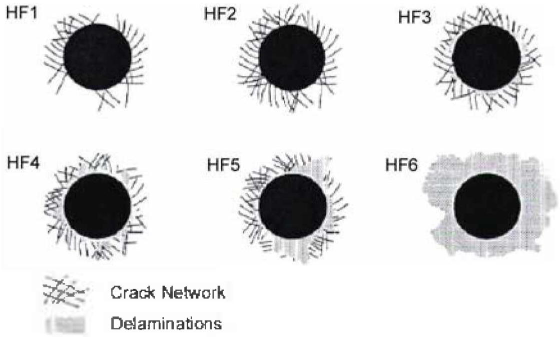

Fig. 3.3: Shape of indents for comparison after coating penetration after VDI guideline 3824.

adhesion for technical applications [25].

3.2.3 XRD Measurements

The measurements were carried out with a Bruker D8 diffractometer in Bragg-Brentano mode between 20 and 80° detector angle and detector scan mode with grazing incidence of 2°. The Cu K_β-radiation was filtered with a SolX-detector. No Ni-filter was used. The operating parameters were kept constant for all measurements and are shown in Table 3.2. The phase identification was conducted by comparing the peak positions measured in $2\,\Theta$ and the relative intensities with the ICDD (International Center of Diffraction Data) powder diffraction files [26].

Tab. 3.2: Operating parameters of Bruker D8 X-ray diffractometer.

λ Cu K_α [Å]	K_β Filter	High Voltage [kV]	Tube Current [A]	Step Time [s]	Step Size 2Θ [°]
1.54056	none	40	30	1.2	0.02

3.2.4 Stress Measurement

To estimate the stress levels at elevated temperatures a laser based optical testing method was used; see Fig. 3.4 [27]. The curvature was assessed by using two parallel He-Ne-laser beams ($\lambda = 632.8\,\mathrm{nm}, 1.2\,\mathrm{mm}$) which were reflected at first by the sample surface and afterwards by a mirror. So the beams were projected to a white surface observable as two points. The distance of these points measured by a slide gauge is proportional to the bending radius of the sample. The samples were positioned in a steel chamber bottom side up to take advantage of the good reflectivity of the Si-wafers. Afterwards the chamber was evacuated to a pressure of 10^{-5} mbar. After starting measurement at room temperature the temperature was raised up to 600 °C in steps of 25 °C. The distance was measured at 25 temperatures during heating as well as during cooling. The bending radius R of the silicon wafers was calculated with

$$R = \frac{2.h.d}{d' - d} \tag{3.2}$$

were h is the distance of the film to the mirror, d is the initial distance between the laser beams and d' is the measured distance after reflection.

The nominal stress was calculated with the modified Stoney equation

$$\sigma_f = M.\frac{t_s^2}{6.t_f}.\frac{1}{R} \tag{3.3}$$

where M is the biaxial modus of the substrate, t_s is the thickness of the substrate, t_f is the thickness of the film and R is the bending radius of the substrate [16, 28].

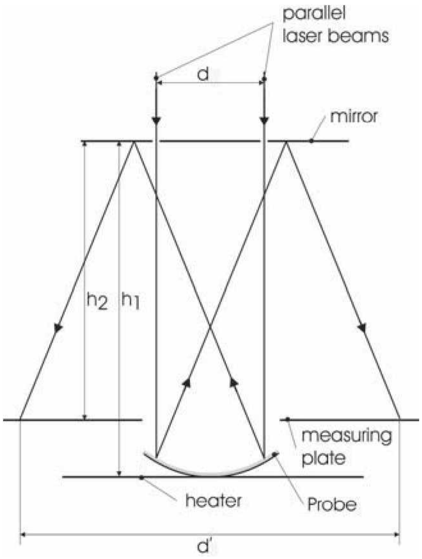

Fig. 3.4: Laser assisted biaxial stress measurement.

3.2.5 Hardness and Young's Modulus Evaluation

Hardness and Young's modulus are commonly evaluated by nanoindentation methods [29]. In literature the indentation depth is commonly adjusted to the $\leq 1/10$ rule of thumb for hardness measurement. In this work the coating thicknesses varied in a range of 1.2 to 3.2 µm because of the different sputter rates for different currents at the vanadium target. So the nanoindentation tests were carried out in two steps: At first, test series with decreasing load starting at maximal load of 50 mN and a step size of 5 mN were done. So a general trend of the hardness and Young's modulus data could be obtained depending on the penetration depth. The optimum measured penetration depth results from fulfilling two important conditions: no noticeable substrate influence and a fully developed plastic zone underneath the indent. In a second step another test with a further reduced penetration depth of 0.08-0.2 µm was carried out to achieve a maximum of accuracy of the Young's modulus. For all measurements a Berkovich indenter with a tip radius less than 0.1 µm was used. Based on the load displacement curve (Fig. 3.5) the hardness was calculated by

$$H = \frac{P}{A}.\frac{Ai}{A} \tag{3.4}$$

where $\frac{Ai}{A}$ means the area function, P is the indentation load and A is the contact area. The Young's modulus was calculated by

$$E^* = \frac{dP}{dh}.\frac{\sqrt{\pi}}{2\beta.\sqrt{A}}.\sqrt{\frac{Ai}{A}} \tag{3.5}$$

where $\frac{Ai}{A}$ means the area function, $\frac{dP}{dh}$ is the stiffness of the material and β is the indenter geometry factor.

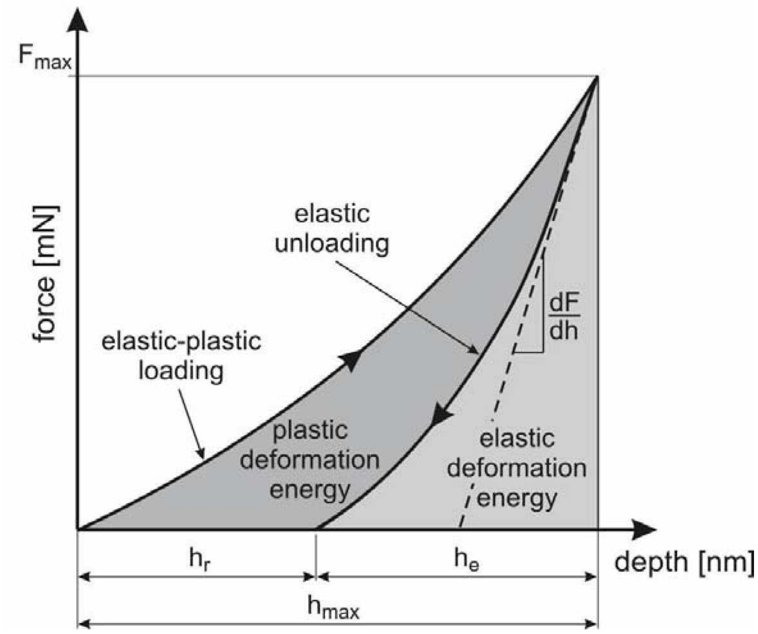

Fig. 3.5: Load-displacement curve resulting from a nanoindentation measurement.

3.2.6 Tribological Investigation

The main point of this work is to obtain specific wear and friction data of the synthesized coatings at RT as well as at elevated temperatures. This was achieved by conducting the so called “ball on disc test” (DIN 50324) using a CSM High Temperature Tribometer as schematically shown in Fig. 3.6.

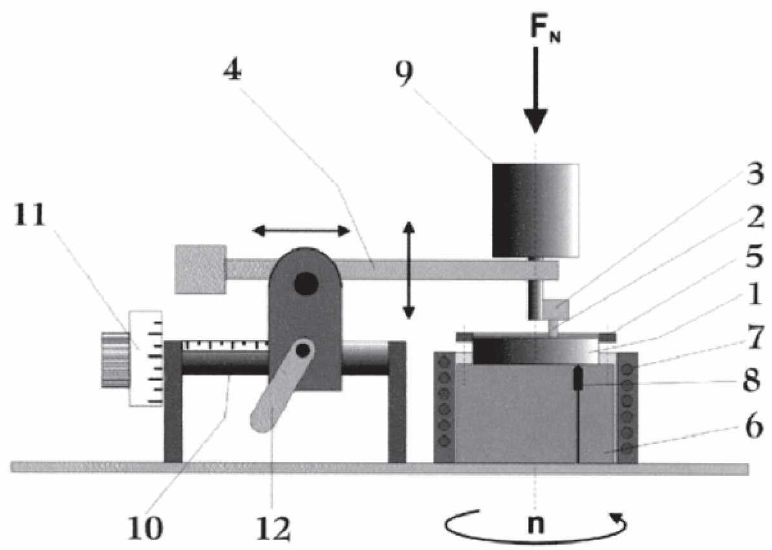

Fig. 3.6: Schematic of ball on disc test showing following components: 1 sample, 2 ball, 3 ball holder, 4 lever, 5 locking ring, 6 rotation cylinder, 7 resistance heating, 8 thermo couple, 9 cylindrical force, 10 axis for adjustable radius, 11 adjusting screw for radius, 12 lock for the lever arm [30].

The coated M2 steel discs were cleaned by an ultrasonic cleaning system for 10 min in acetone and 10 min in ethanol and fixed by a locking ring on the afterwards rotating cylinder. The temperature can be adjusted up to 800 °C by a resistance heater around the rotation cylinder. Additional heating can be applied due to an ohmicly heatable cover plate in a distance of about 40 mm beyond the sample surface.

The most important parameters for evaluating and comparing friction data are listed below comprehending the specific data used for this work [31, 32] :

1. Friction Partner: Al_2O_3 ball, $\varnothing$6 mm
2. Linear Sliding Speed: 10 cm/s
3. Normal Load: 2 N (dead weights made of steel using polymer rings between weight and lever to absorb vibrations)

4. Temperature: RT (25 °C), 600 °C, 800 °C

5. Radius of Wear Track: 7 mm

6. Sliding Distance: 500 m (≈10000 laps) for RT, 100 m (≈2000 laps) for elevated temperatures

7. Environment: Dry air (Humidity 40±5 %)

8. Acquisition Rate: 10 Hz

The Al_2O_3 ball was cleaned with ethanol and fixed in a pin-ball holder made of Inconel. The sliding distance was adapted to the overall performance of the coatings. The coefficient of friction (COF) was evaluated recording the data of the tangential friction force from a Linear Voltage Displacement Transducer (LVDT) which measures the deflection of the cantilever assembly that holds the pin/ball. Using the equation of friction

$$\mu_R = \frac{F_T}{F_N} \tag{3.6}$$

where F_T is the tangential force at the lever and F_N is the normal load of the dead weight, the COF is calculated by the software.

3.2.7 Optical Profilometry

Different grain growth due to different deposition parameters leads to different grain size and/or orientation which may change surface conditions like roughness and optical appearance. For surface sensitive investigation methods like nanoindentation or tribological testing the surface roughness shows a strong influence on the accuracy. The surface roughness of all coatings was determined by an optical white light profilometer (Veeco Instruments Wyko NT 1000) Fig. 3.7 [33, 34]. Also the wear tracks of the tribological test were investigated in detail. For the characterization of the surface roughness the roughness average R_a (arithmetic roughness) was used which is given by

$$R_a = \frac{1}{MN} \cdot \sum_{j=1}^{M} \sum_{i=1}^{N} |Z_{ji}| \tag{3.7}$$

where M and N designate the number of data points in the x- and y-direction and Z is the surface height relative to the reference mean plane.

For all measurements the vertical scanning interferometry (VSI) mode (Full resolution, 1x speed, Backscan 5 µm, Scanlength 12 µm, Objective (2.5-10 x), Field of view (FOV) 1.0 x, Modulation Threshold 0.1 %) was used where it is possible to achieve a vertical resolution of 3 nm at a maximum scan length of 1 mm. So it was possible to detect general variations in overall profile height characteristics.

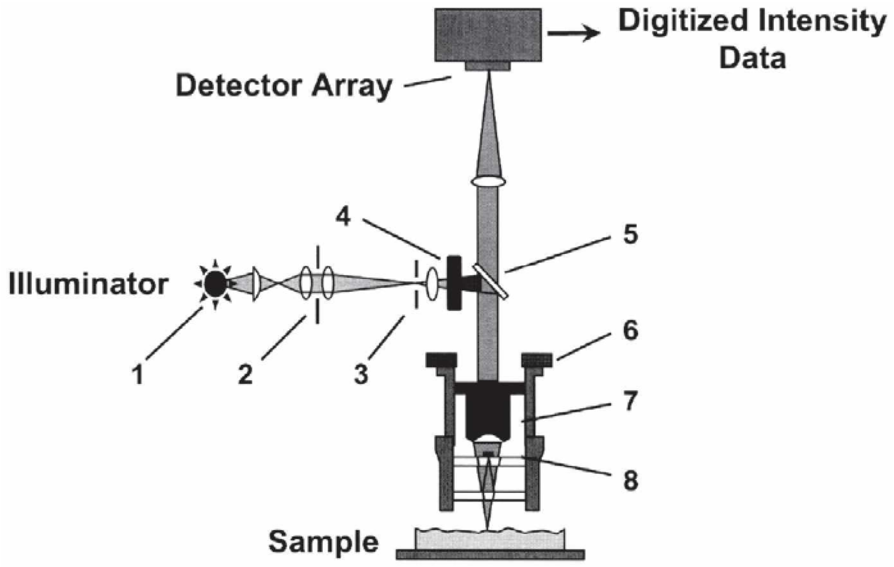

Fig. 3.7: Schematic of the visible light profilometer: 1 light source, 2 aperture stop, 3 field stop, 4 filter, 5 beam splitter, 6 translator, 7 microscope objective, 8 Mireau interferometer.

In case of one sample after high temperature tribological measurement the surface was oxidized and very rough. No optical profilometry could be conducted and the wear tracks were characterized using the "NanoFocus-µ-surf" confocal microscope provided by MCL (Materials Center Leoben) instead.

3.2.8 Scanning Electron Microscopy

The investigation of the wear tracks was carried out with a scanning electron microscope (Zeiss EVO50 SEM) with an acceleration voltage of 15 kV. The elemental composition in the wear tracks and of the V-containing coatings was evaluated by energy dispersive X-ray spectroscopy (Oxford Instr. INCA EDX).

3.2.9 Raman Spectroscopy

V-compounds like V_2O_5 or VO_2 which are expected to be dispersed in the ZrO_2 matrix are Raman active. This means that monochromatic light, usually from a laser in the visible, near infrared, or near ultraviolet range interacts with phonons or other excitations in the atomic system (Fig. 3.8).

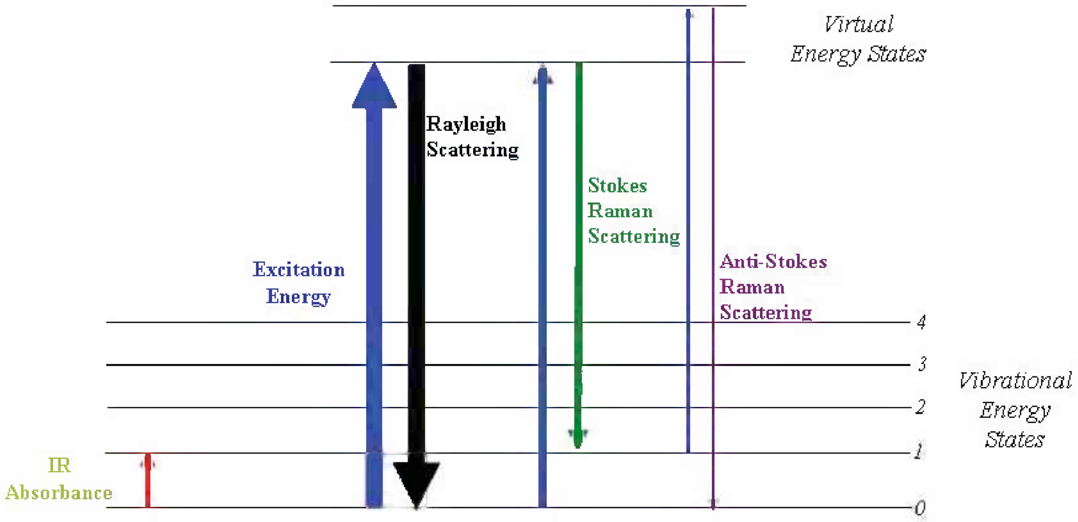

Fig. 3.8: Photon-Phonon interaction of Raman spectroscopy measurements [35].

Raman spectroscopy was used to detect small volume fractions of V-compounds that may not be detected by XRD. Raman spectroscopy can be understood as inelastic scattering of photons with molecules [36]. The energy of the laser photons is shifted up or down. This shift in energy gives information about the phonon modes in the system which can be related to the according compound or material structure. Raman spectroscopy measurements were conducted using a Horiba Dilor Raman spectroscope with a laser wavelength of 532.2 nm (Nd:YAG laser) at a power level of 100 mW (3.5 mW at the measured spot). The recorded spectra were compared with a database containing reference spectra.

3.2.10 DSC-Measurements

Three different coating compositions were also synthesized on Fe-foils. The foils were dissolved in an aqueous solution of 15 % HNO_3 at 70 °C. The dissolution was finished when the powder in the solution showed no attraction to a strong magnet which was placed near the test glass. Just pure powder of the coating remained after filtration which was washed in ethanol and dried in air. Before DSC measurements were conducted the produced powders were investigated by XRD for any significant changes due to the dissolution treatment. The measurements were conducted with a LAPSYS EVO DSC measurement system in synthetic air to allow oxidation reactions to take place. The flow rate was 20 cm^3/min at a heating rate of 20 K/min. The temperature range was chosen between RT and 1000 °C.

4 Results and Discussion

4.1 Coatings as Deposited

4.1.1 Constitution and Chemical Composition

Chemical Composition

The EDX spectra of coatings with three different V-contents are shown in Fig. 4.1. The elemental compositions of V, Zr, O and Fe which originates from the M2 substrate (outlined in Table 4.1) show that the V-contents are 2.2 at%, 5.8 at% and 17.4 at%. Because of the low conductivity of the coatings these values do not show an accuracy as good as commonly achievable with this method. With V-content increasing from 2.2 at% up to 17.4 at% ($\Delta = 15.12$ at%), the Zr-content decreases from 33.3 at% to 23 at% ($\Delta = 10.3$ at%) while the O-content remains nearly constant ($\Delta = 4.63$ at%). If the stoichiometric relations between Zr-O and V-O are considered, which are in high

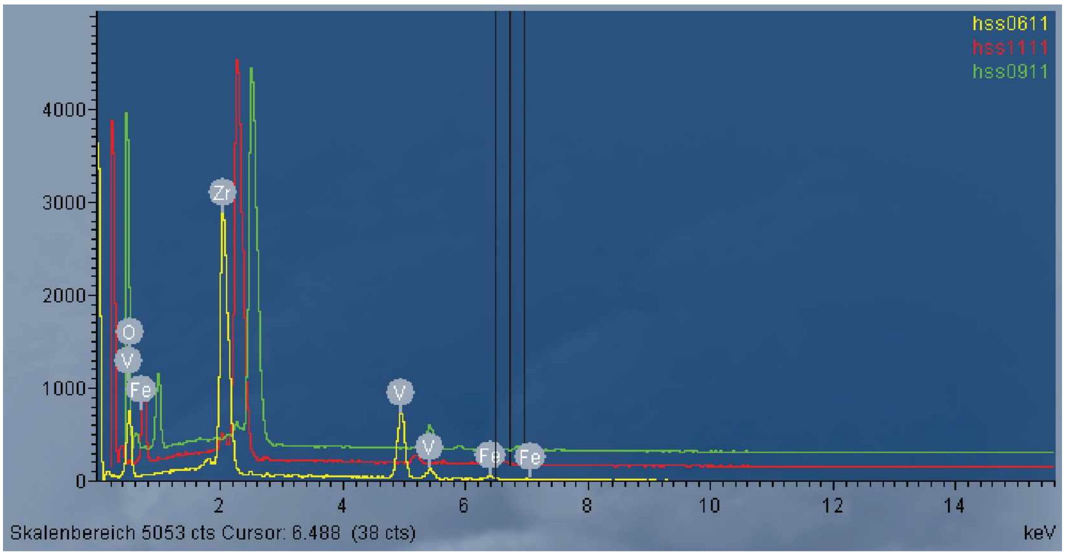

Fig. 4.1: EDX spectra of ZrO_2 coatings synthesized with varying currents on the V-target.

oxidation states like ZrO_2 and V_2O_5, it has to be mentioned that the O-fraction in the coating is low.

Tab. 4.1: Contents of V, Zr and O of ZrO_2 coatings synthesized with varying currents on the V-target. The measured Fe signal originates from the M2 substrate.

Substrate	Current density on V-target [mA/cm^2]	O**	Zr**	V**	Fe**
M2	4.1	63.5	33.3	2.2	1
M2	7.6	61.1	31.8	5.8	1.4
M2	17.8	58.9	23	17.4	0.8

**All values are given in atomic percent [at%]

Phase Analysis

X-ray diffraction experiments are performed on coatings deposited on M2 steel discs, Si-wafers with (100) orientation and on Fe-foils in Bragg-Brentano mode. Diffractograms on Si and M2 are shown in Fig. 4.2 and Fig. 4.3. Independent of the substrates a general trend is visible: For the undoped ZrO_2 and the coating with the lowest V-content of 2.2 at%, monoclinic ZrO_2 can be identified as the dominant phase. At a higher V-content of 5.8 at% all X-ray diffraction peaks can be attributed to cubic/tetragonal ZrO_2 and at even higher V-content of 17.4 at% the coating becomes X-ray amorphous. It has to be mentioned that no peaks of vanadium compounds could be identified with reasonable certainity. Also Fateh et al. showed that reactive magnetron sputtered V_2O_5 films cannot be clearly identified by XRD below a deposition temperature of 300 °C because lower temperatures do not provide sufficient thermal energy for ad-atom mobility which results in an amorphous structure [37]. Furthermore there is a valence reduction at elevated temperatures in vacuum atmosphere from V_2O_5 to VO_2 [13]. Zheng Liu et al. showed also an influence of increasing V-contents on the morphology of the ZrO_2 matrix from monoclinic to cubic/tetragonal. With XRD methods it cannot be shown how the V is incorporated in the ZrO_2 matrix. Most likely, it is dispersed as an amorphous or nano crystalline phase like already shown in the structure model of chameleon coatings by Voevodin and co-workers [1], but no experimental proof can be found within this work. It should be noted that there is one peak at about 45 ° on the M2-substrates as well as on the Si-wafers which cannot be identified by comparing with the ICDD powder diffraction files.

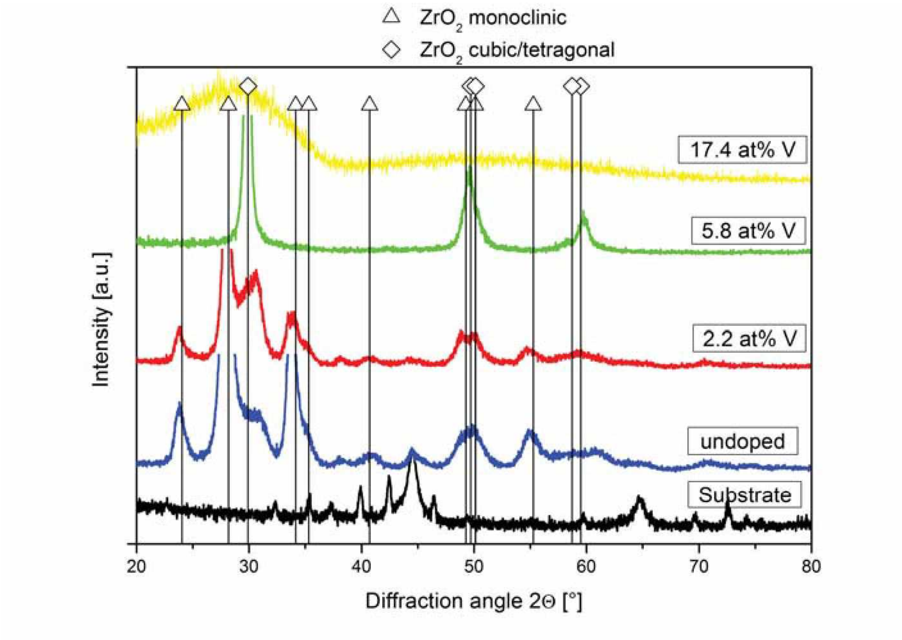

Fig. 4.2: XRD pattern showing the change of structure from monoclinic to cubic/tetragonal ZrO_2 with increasing V-content on M2 substrates.

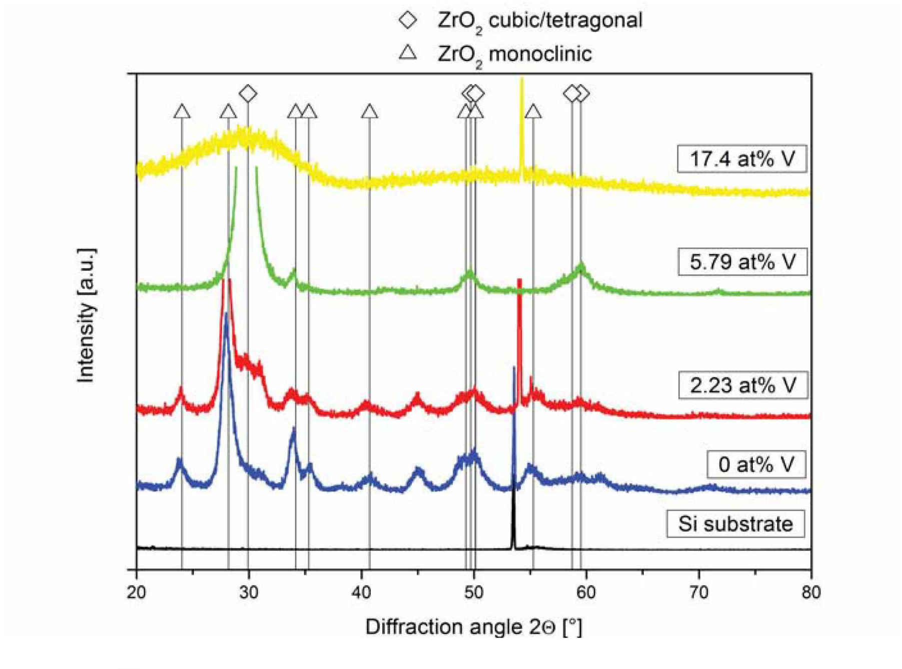

Fig. 4.3: XRD pattern showing the change of structure from monoclinic to cubic/tetragonal ZrO_2 with increasing V-content on Si (100) substrates.

Fig. 4.4 and Fig. 4.5 compare the XRD patterns before and after dissolution of the Fe-foils to exclude phase transitions or reaction processes during dissolution in 15 % HNO_3 for preparing the powder for the DSC measurements. The peak at 45 ° from the Fe-foil can not be detected in the powder any more which indicates a complete dissolution of the substrate.

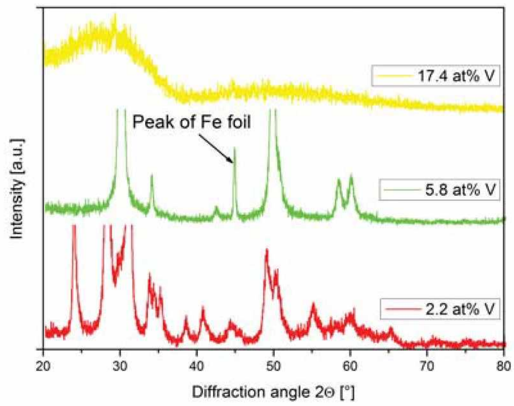

Fig. 4.4: XRD pattern of Fe-foil coated with ZrO_2 films with different V-contents.

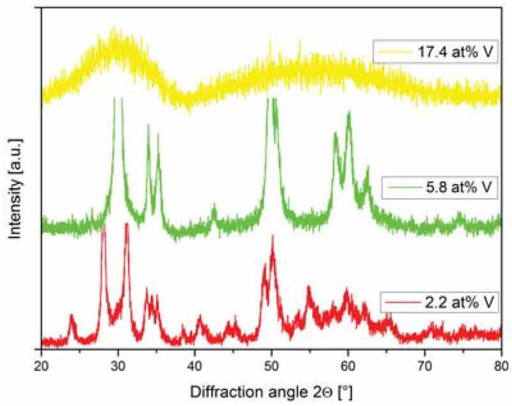

Fig. 4.5: XRD pattern of the coating powder after dissolution of the Fe-foil.

Raman spectroscopy is conducted because no V-component can be shown by XRD. The Raman spectrum of a coating with 17.4 at% deposited on a Si-wafer at 150 °C, which is X-ray amorphous (see Fig. 4.3), is shown in Fig. 4.6.

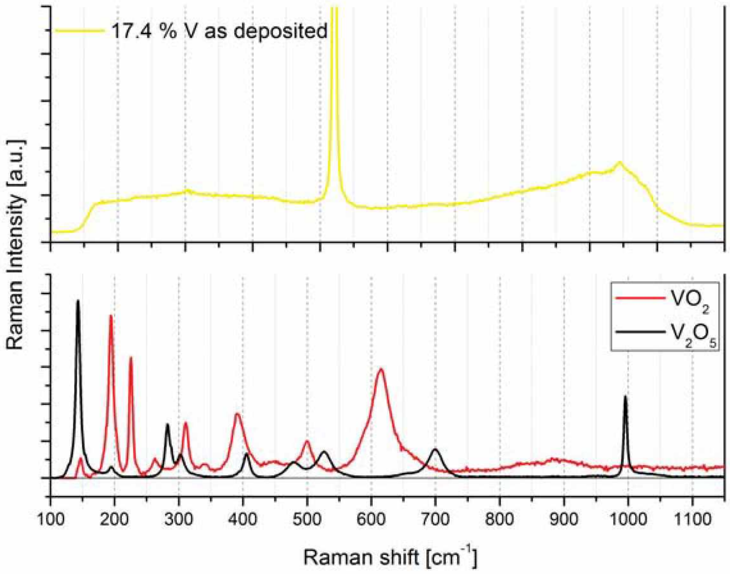

Fig. 4.6: RAMAN spectrum of a ZrO_2 film with 17.4 at% V and reference spectra for V_2O_5 and VO_2 taken from [38].

Just one significant peak at about 520 cm^{-1} is detected which can be clearly identified as silicon [39]. The pattern of V_2O_5 and VO_2 are given as reference [38]. No peak which designates a V-O compound can be observed in the as deposited state.

Coating Thickness

Possible residual stresses of the coating and the interpretation of the results of nanoindentation, especially of the Young's modulus evaluation, are strongly influenced by the coating thickness. Coating thicknesses >1 µm are required for a reasonable characterization. The deposition time is adapted so that all coating thicknesses are above 1 µm. The determined coating thicknesses are listed in Table 4.2. The current density on the Zr targets was kept constant at 17.6 $\mathrm{mA/cm^2}$. The current density of the V target was varied from 0 to 17.6 $\mathrm{mA/cm^2}$. In case of a V target current density of 17.6 $\mathrm{mA/cm^2}$ the contribution of the V target to the total growth rate of the film is around 50 %. This means that the contribution of one V target to the coating thickness is 200 % compared to that of one Zr target. This value is confirmed by the thicknesses of the undoped coating and the coating with 17.4 at% V.

Tab. 4.2: Coating thicknesses of ZrO_2 films with V added depending on deposition parameters.

Sample	Zr-targets	V-target	I_V [$\mathrm{mA/cm^2}$]	Deposition time [min]	Coating thickness [µm]
undoped	3	0	0	240	2.3
2.2 at% V	2	1	4	360	1.7
5.8 at% V	2	1	7.6	240	1.2
17.4 at% V	2	1	17.6	240	3.1

Surface Roughness

The mean surface roughness R_a determined by optical profilometry of all coatings as deposited is nearly constant with 10±2 nm. As one characteristic example, the surface of a coating deposited at 150 °C for 240 min with 5.8 at% V is shown in Fig. 4.7.

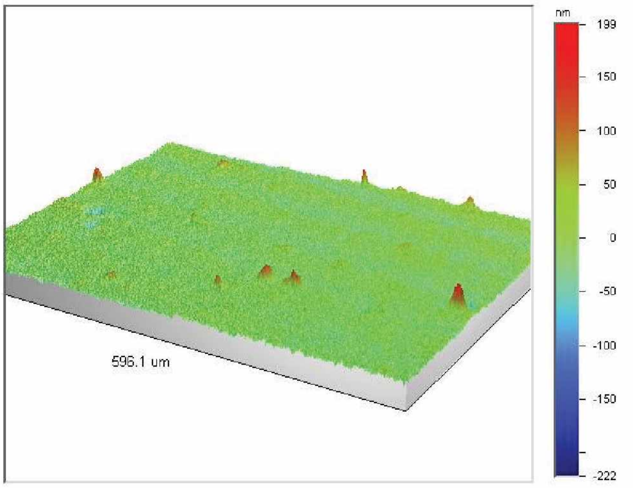

Fig. 4.7: Surface of a ZrO_2 film as deposited with 5.8 at% V.

4.1.2 Mechanical Properties

Coating Adhesion

Fig. 4.8 to Fig. 4.10 illustrate the coating adhesion determined by Rockwell-C indentation. Good adhesion is crucial for coating performance, especially under mechanical and thermal load.

Compared to the VDI guideline 3824 for Rockwell-C testing, the films are not well adherent with a HF number of 4-5. An adequate interlayer may be required to increase the adhesion but this is out of the scope of this work.

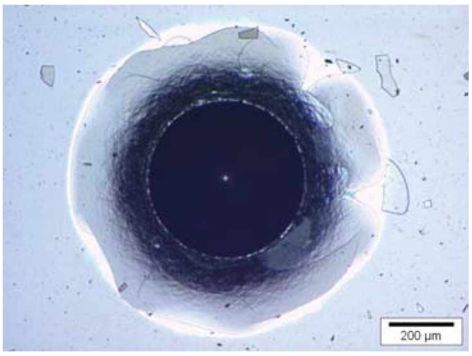

Fig. 4.8: Rockwell-C indent on the undoped ZrO_2 coating.

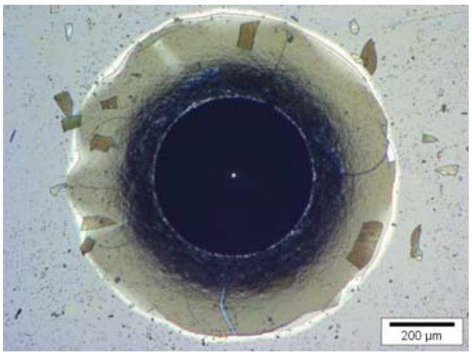

Fig. 4.9: Rockwell-C indent on the coating with 2.2 at% V.

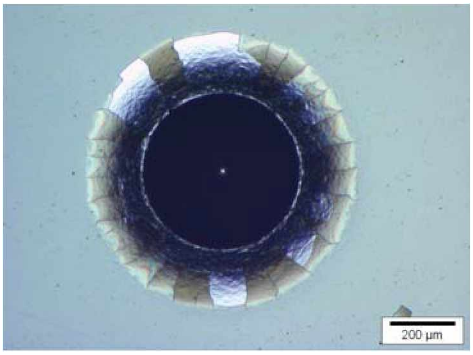

Fig. 4.10: Rockwell-C indent on the coating with 5.8 at% V.

Hardness and Young's Modulus

The change of the coating structure and composition due to the incorporation of V will affect the overall mechanical properties such as hardness and Young's modulus. Sputtered ZrO_2 thin films are reported to have a hardness of 19 GPa and a Young's modulus of 210-231 GPa [5] which will provide good mechanical stability. V compounds show quite low values in hardness and Young's modulus compared to ZrO_2 and will decrease the overall mechanical stability. The hardness of the undoped ZrO_2 and of the coatings with three different V-contents is shown in Fig. 4.11. For V-contents up to 2.2 at%, the monoclinic ZrO_2 is the dominant phase with a hardness of 17.3 GPa (without V) and 17.6 GPa (with 2.2 at% V). The hardness remains nearly constant for V-contents up to 5.8 at% (17.1 GPa), where already a cubic structure was obtained. At higher V-contents of 17.4 at%, a significant decrease of the hardness (7.4 GPa) occurs.

The same trend can be affirmed for the Young's modulus values shown in Fig. 4.12. The Young's modulus measured for ZrO_2 is 240 GPa. For small V values of 2.2 at%, the Young's modulus is nearly constant (235 GPa). For higher V-contents a decrease of the modulus to 220 GPa can be seen. The Young's modulus for even higher V-contents of 17.4 at% decreases rapidly to 150 GPa.

The coating with 17.4 at% V shows a structure which is X-ray amorphous as deposited (Fig. 4.2). It can be assumed that the long range order and crystal structure stability of the ZrO_2 matrix, which is caused by the bonding strength of oxide ceramics (70% ionic, 30% atomic) [40], is disturbed by high contents of V-O which results in a nanocrystalline, amorphous or glassy structure with deteriorated mechanical properties.

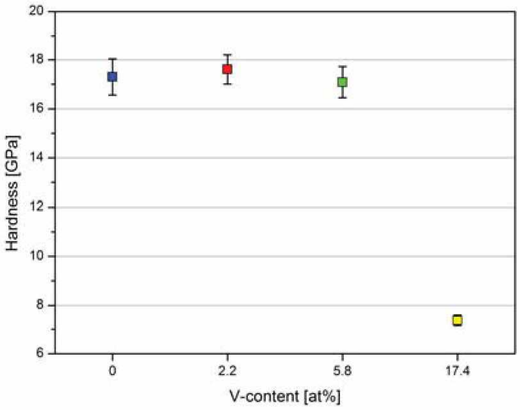

Fig. 4.11: Hardness depending on the V-content of ZrO_2 films.

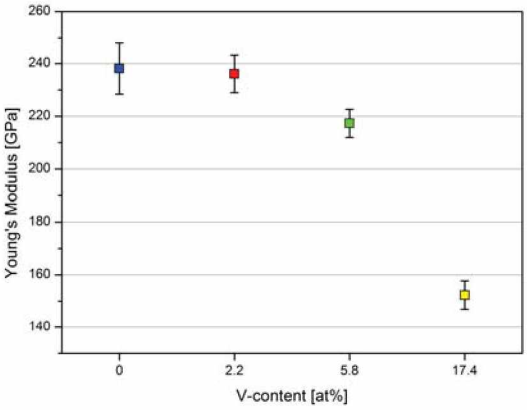

Fig. 4.12: Young's modulus depending on the V-content of ZrO_2 films.

4.2 Tribological Performance

The coating design concept of this thesis is targeting multifunctional sliding properties over a wide temperature range. Thus, tribological tests are performed at RT, at 600 °C and at 800 °C. The coatings shall combine resistance against wear and abrasion due to their hardness and good sliding properties based on a self lubricious nature at temperatures up to 800 °C. It shall be illuminated if there is a tendency of beginning self lubricious low friction effects on the coating surface caused by temperature increase or applied load. If the coating had a nanocomposite structure like that proposed by Voevodin and co-workers, showing a matrix of a hard crystalline zirconia phase including dispersed nanocrystalline V-compounds, it might be possible to squeeze out the molten V_2O_5 under applied load and temperatures $\geq 550\,^{\circ}C$ to form a sliding film in the wear track. Such effects caused by diffusion have already been shown by Hu et al. on Ag doped zirconia multilayers which provided low friction coefficients of 0.4 or less for more than 25000 cycles [4].

4.2.1 Room Temperature

The parameters of the testing procedure at RT are adapted to the performance of the undoped ZrO_2 film. In the first set of experiments different loads are applied to the ZrO_2 coating to evaluate the adequate load to achieve a sliding distance of 10000 laps at room temperature without coating failure and substrate contact. According to these tests a load of 2 N is chosen for RT testing.

Fig. 4.13 shows the friction behavior of the undoped ZrO_2 coating compared with the V containing coatings at RT. The mean coefficient of friction μ_R of the undoped ZrO_2 coating tested at a normal load of 2 N is 0.24 over the whole sliding distance of 10000 laps.

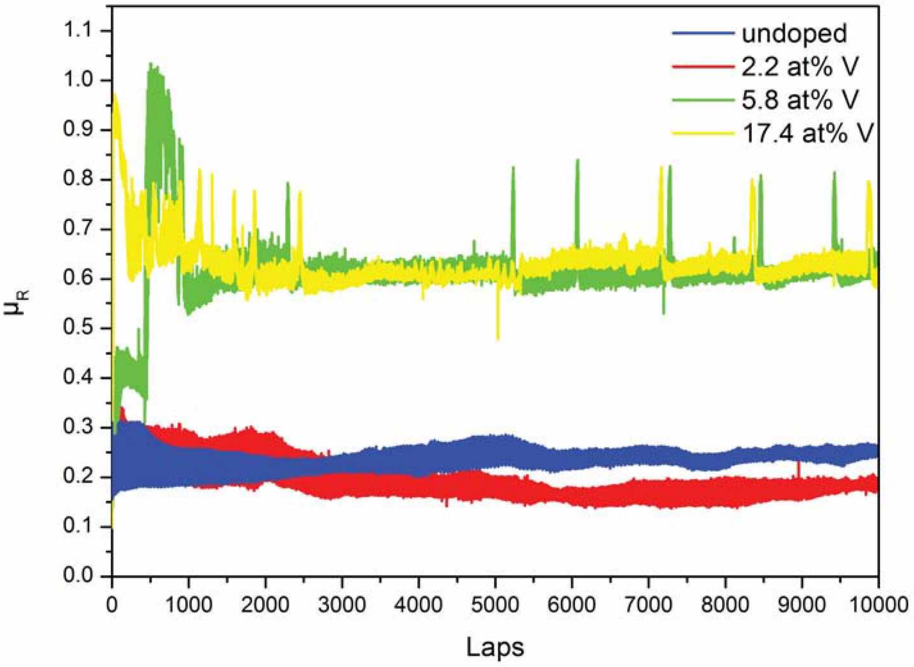

Fig. 4.13: Friction curves at room temperature for undoped ZrO_2 and three different V-contents.

Compared to the undoped coating there is a decrease of μ_R at small V contents of about 2.2 at% to a value of 0.19. At an elevated V content of 5.8 at%, μ_R increases up to 0.4 showing first failure in the wear track after ≈430 laps which can be seen in a sudden increase to $\mu_R = 1.04$ and a decrease to 0.65 up to 10000 laps. The coating with the highest V content of 17.4 at% shows a relatively high friction coefficient of 0.7 during the run-in period and afterwards a decrease of μ_R down to 0.65 up to 1000 laps.

The relation between the hardness of the coating and the friction partner may influence the overall tribological performance [41]. On a hard coating, the load will be supported by the coating and lead to a small contact area. Consequently low friction is obtained for the coatings with a V-content up to 2.2 at%. When the hardness of the coating is relatively low, ploughing and shearing will occur which leads to an increased contact area, higher friction coefficients, severe abrasion and material loss which is the case for the amorphous coating with 17.4 at% V with early coating failure. The combined parametric ratio H/E, where H designates the hardness and E the Young's modulus, has a relationship to the general tribological performance of a coating [42]. This ratio describes the ability of a coating to deflect with the substrate in a reversible elastic way (low Young's modulus values) and the resistance against abrasion (high hardness values). The ratio of H/E is nearly constant for the undoped coating (0.0727), the coating with 2.2 at% V (0.0745) and the coating with 5.8 at% (0.0787). There is only a significant decrease of H/E for the coating with 17.4 at% (0.0485) which is only 66 % of the highest ratio obtained for the coating with 5.8 at% V.

The profiles of the wear tracks after 10000 laps at room temperature and a normal load of 2 N vary with different V-contents in a wide range (Fig. 4.14). The undoped coating shows a good performance with a small wear track depth of 0.7 µm. For a V-content of 2.2 at%, the coefficient of friction decreases to the lowest value measured of about 0.19. The wear track depth is extremely low with 0.2 µm only observable by optical microscopy and profilometry. For even higher V-contents of 5.8 at% V, the wear

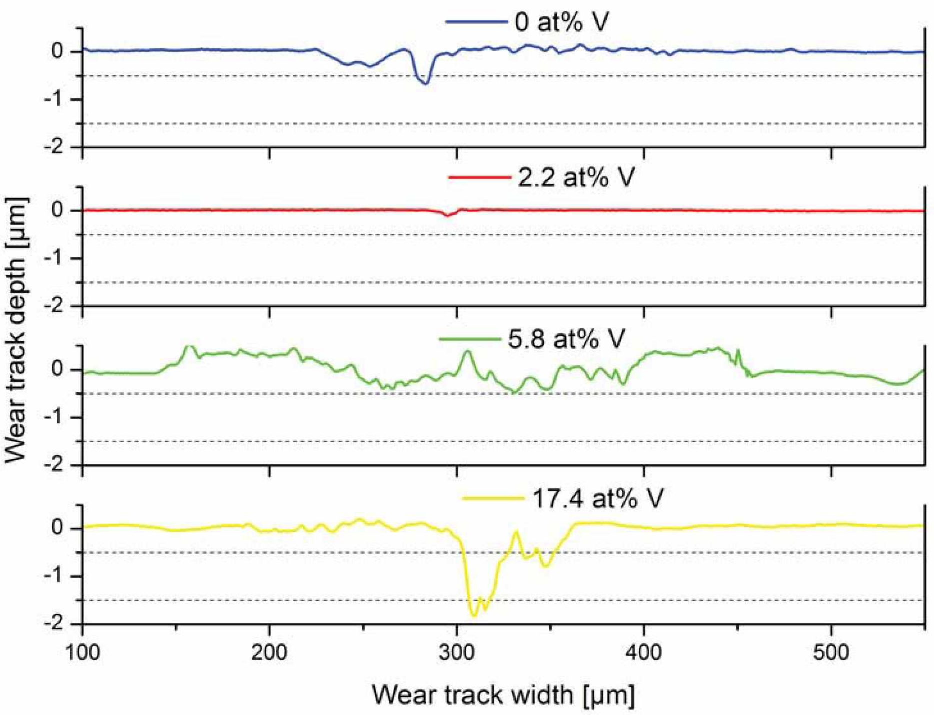

Fig. 4.14: Wear track profiles after 10000 laps with 2 N normal load at RT.

track width increases drastically while the depth reaches a value of 0.45 µm. This may be caused by the high ratio of H/E meaning higher elastic deformation of the coating under load, which leads to a higher contact area between ball and coating, lower contact pressures and decreasing wear track depths. The wear track at a V-content of 17.4 at% shows a maximum depth of 1.9 µm which comes already close to the overall coating thickness of 2.3 µm evaluated for this coating. The ratio of H/E is the lowest measured, indicating low resistance against abrasion and thus high wear track depths.

After room temperature tribological testing, the wear tracks are examined by SEM to evaluate if there are any indications for self lubricious effects at low temperatures in the wear tracks (Fig. 4.15 to Fig. 4.18). For all coatings, there is no evidence for self lubricious effects like smeared wear tracks. The borders of the wear tracks look brittle and frayed.

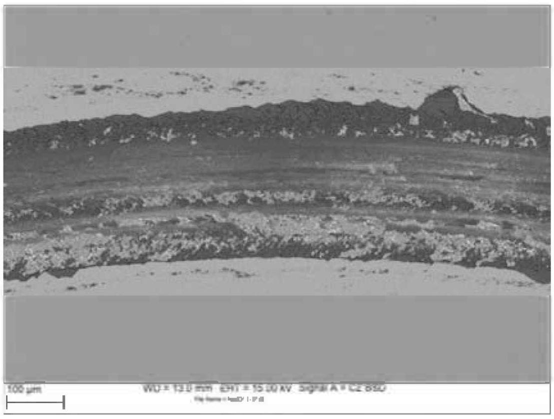

Fig. 4.15: SEM micrograph of the wear track on the undoped ZrO_2 coating.

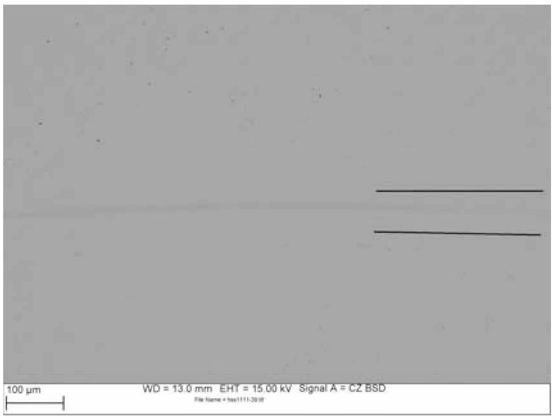

Fig. 4.16: SEM micrograph of the wear track on the ZrO_2 coating with 2.2 at% V.

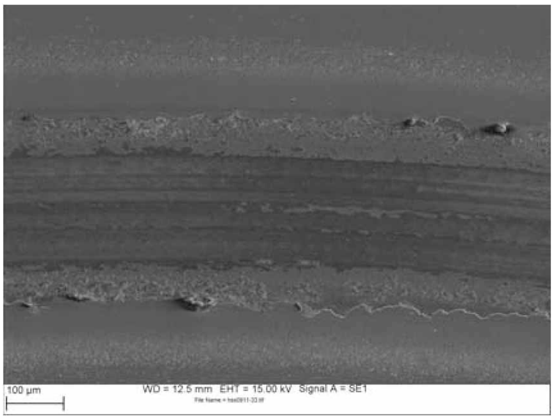

Fig. 4.17: SEM micrograph of the wear track on the ZrO_2 coating with 5.8 at% V.

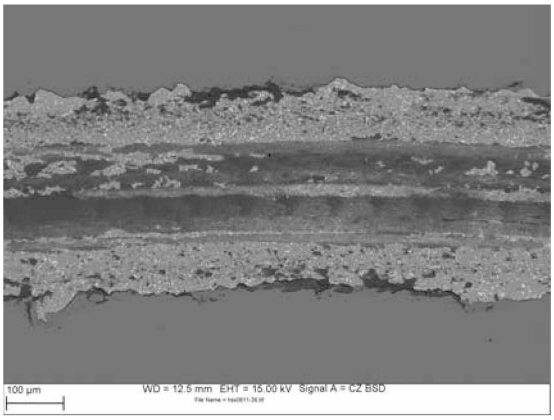

Fig. 4.18: SEM micrograph of the wear track on the ZrO_2 coating with 17.4 at% V.

4.2.2 High Temperature

The aim of the high temperature testing at 600 °C is to determine if there are low melting V-O compounds which provide low friction behavior caused by the easy shearing lattice planes of solid dispersed phases like V_2O_5 or due to forming a sliding film of molten V_2O_5. The normal load is again kept constant at 2 N to afford an easy comparability of the two temperature ranges while the sliding distance had to be reduced to 2500 laps because coatings tend to fail earlier. The friction curves of the coatings obtained at 600 °C are shown in Fig. 4.19. The black curve designates the tribological performance of the substrate to verify coating failure and ball-substrate contact by comparing the particular friction plateaus. It is recognizable that the friction coefficient of the substrate and the coating with 2.2 at% V scatter in a similar and relative wide range and their plateaus are situated at the same level. This is an indication for early coating failure and substrate

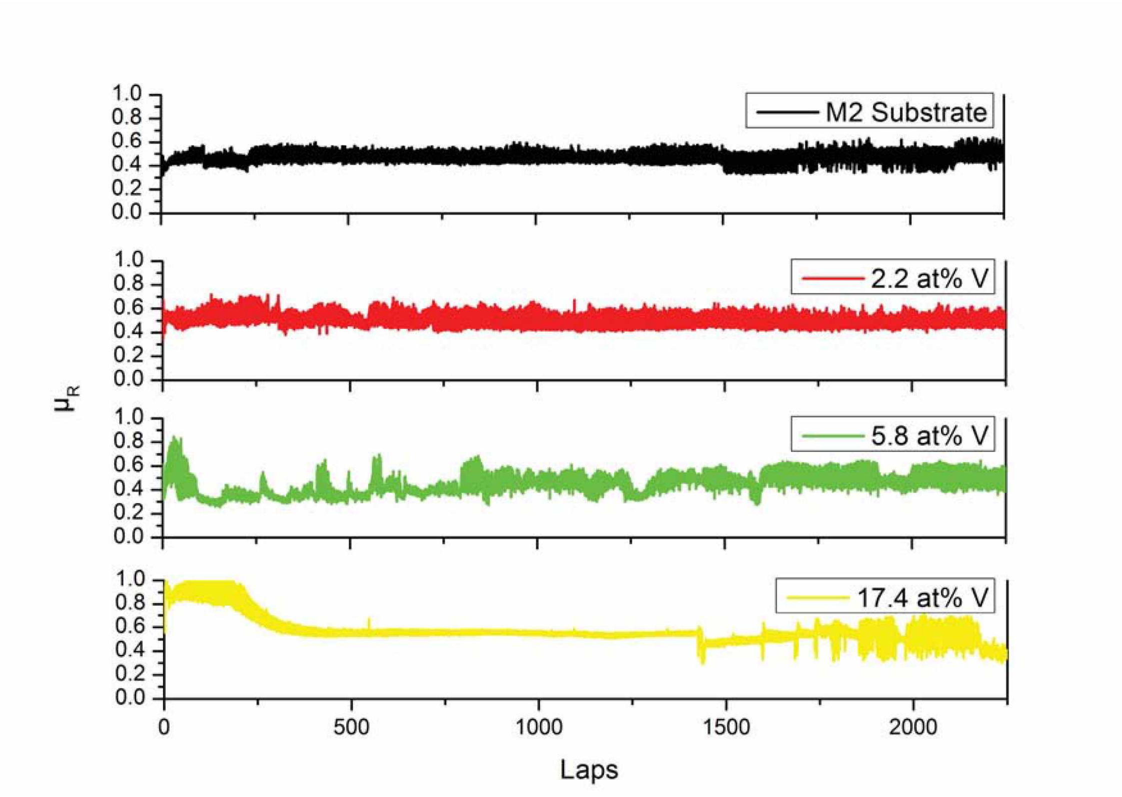

Fig. 4.19: Tribo-curves at intermediate temperature (600 °C) for the M2 substrate compared to the ZrO_2 coatings with three different V-contents.

contact. The sample with 5.8 at% V shows at the beginning high friction for a distance up to about 50 laps but then a plateau with the lowest friction value of about 0.35 up to 750 laps was obtained. After 750 laps, the friction coefficient increases to 0.45 until coating failure at about 1600 laps occurs. The curve shows a jagged characteristics which is an indication that abrasive particles are piled up in front of the Al_2O_3 ball which lead to an increase of the friction coefficient. When breaking free, the coefficient of friction decreases rapidly again. The coating with 17.4 at% V shows the lowest scattering of μ_R but a quite high plateau of 0.55 up to 1500 laps, after very high values up to 1 during the running-in period. This sample shows no coating delamination up to sliding distances of close to 1500 laps. According to its H/E ratio, the sample with 17.4 at% V is assumed to be tough which could be a reason for better adhesion without crack formation due to mechanical and thermal stresses. Nevertheless it has to be mentioned that also this coating is not able to withstand the normal load for the whole sliding distance, as indicated by the increased scattering after 1500 laps. The 3 D image of the wear track of the sample with 17.4 at% V is shown in Fig. 4.20. The wear track reaches

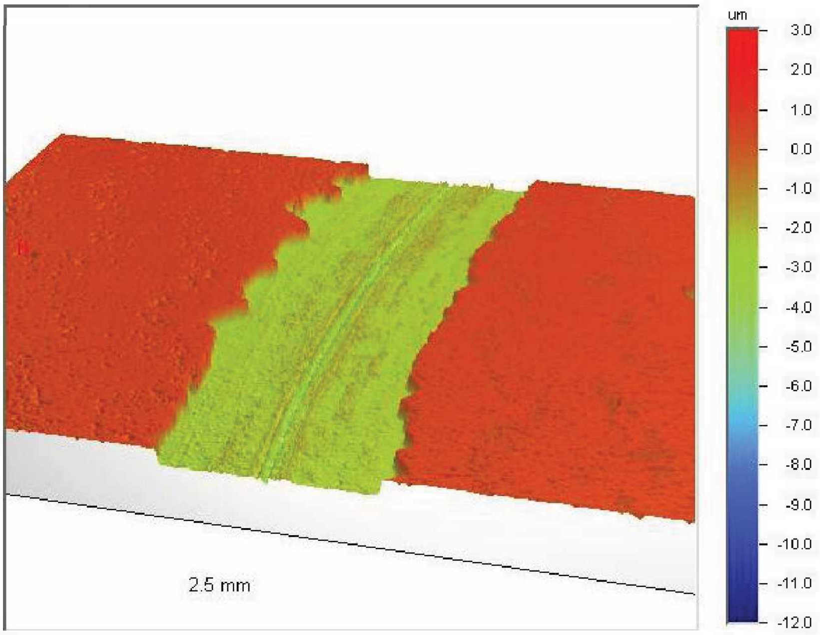

Fig. 4.20: 3D wear track profile obtained by ball-on-disc testing for 1500 laps with 2 N normal load at 600 °C.

already the substrate material. It can be seen in Fig. 4.19 that coating failure occurred after 1500 laps. The shape of the wear track flanks allows some conclusions about the material behavior and the adhesion between coating and substrate. In this case, the flanks of the wear track plunge down abruptly. On the ground of the wear track no coating material is left. This is an indication for brittle behavior with a tendency of bad coating adhesion over the whole wear track.

Except for the undoped sample and that with 17.4 at% V, there is a general trend of total or partial coating delamination as shown in Fig. 4.21. For the undoped coating this can be explained because of the unique linear thermal expansion coefficient of ZrO_2 of α=10.3 × 10^{-6} m/K [43], which is close to that of the M2 steel (11.5-13 × 10^{-6} m/K), and the absence of volume changes due to phase transformations up to this temperature.

Visual inspection indicates that coating delamination of the sample with 5.8 at% V occurs after the tribological test during cooling down to RT at about 150 °C while for the coating with 2.2 at% V delamination happens when the load is applied.

To investigate if coating delamination is caused by the development of stresses due to thermal expansion, the biaxial stress levels of the coatings depending on the V content are measured in the temperature range from RT up to 600 °C on silicon substrates in vacuum. The calculated stress levels are shown in Fig. 4.22.

The coating with 2.2 at% V failed because of crack formation and is thus not included

Fig. 4.21: Delamination of the coating with 5.8 at% after tribo-testing at 600 °C.

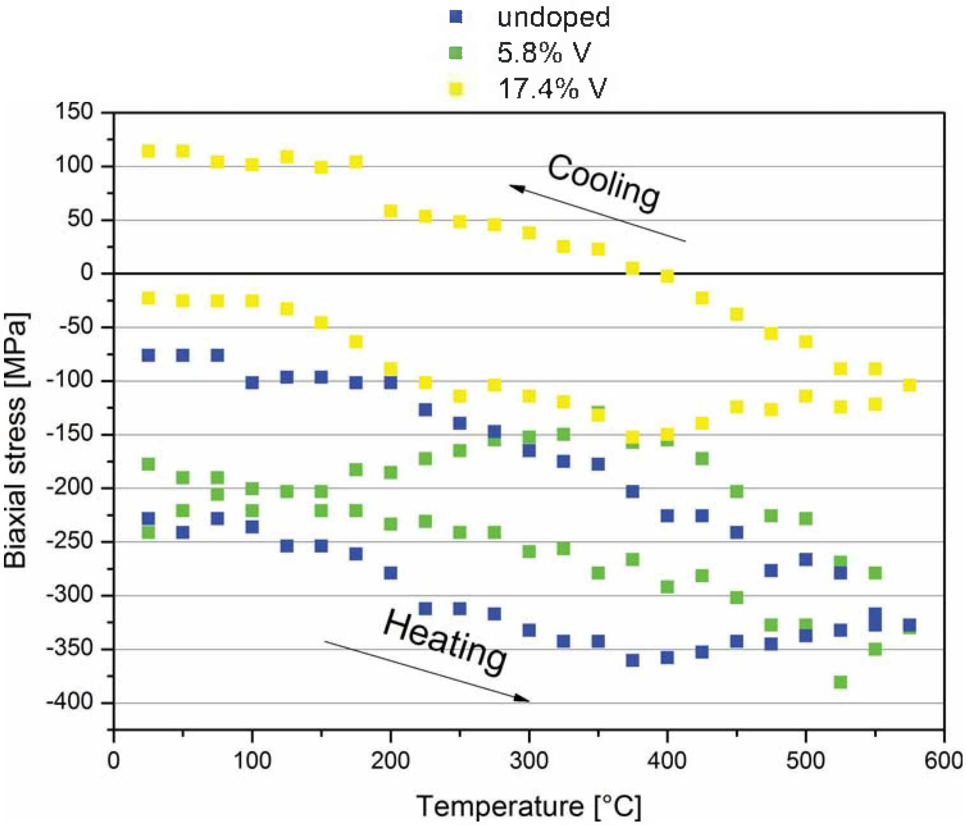

Fig. 4.22: Biaxial stress levels in the temperature range from RT up to 600 °C of the undoped ZrO_2 coating compared to those with two different V-contents.

in Fig. 4.22. As deposited, all stress levels on the silicon substrates are compressive and inrease with increasing temperature. Up to 150 °C, which is the deposition temperature for all coatings, the stress levels are nearly constant. Up to 400 °C, the compressive stress increases because of the different thermal expansion coefficients (2.6×10^{-6} m/K for the Si wafer [44] and about 10.3×10^{-6} m/K for the ZrO_2 coating [43]). Above 400 °C, out-annealing of defects, crystallization and grain growth are assumed to be dominant, thus the compressive stresses decrease. The highest compressive stress is -360 MPa measured for the undoped ZrO_2 coating at 375 °C. After reaching the highest temperature of 575 °C, the compressive stress decreases to minus 350 MPa for the undoped coating and for the coating with a V content of 5.8 at%. After cooling down to RT, the compressive stresses decrease to -76 MPa for the undoped coating and to -175 MPa for the coating with 5.8 at% V. The coating with the highest V-content of 17.4 at% shows the lowest compressive stress at 575 °C (-100 GPa) and tensile stress after cooling down to 375 °C. The stresses decrease with increasing V-content. In general these biaxial stresses are low compared to other coating systems (see [45]) and may thus not be the only activator for coating delamination at elevated temperatures. However, it has to be mentioned that the thermal expansion coefficients of Si-substrates (3×10^{-6} m/K) may not allow an easy comparison to tribological testing conditions on M2 steel ($11.5\text{-}13 \times 10^{-6}$ m/K).

The XRD pattern of the coating containing 17.4 at% V after a tribological test at a temperature of 600 °C is shown in Fig. 4.23, indicating formation of the mixed oxide phase ZrV_2O_7. The peaks at 30°, 50° and 60° are identified as cubic/tetragonal ZrO_2.

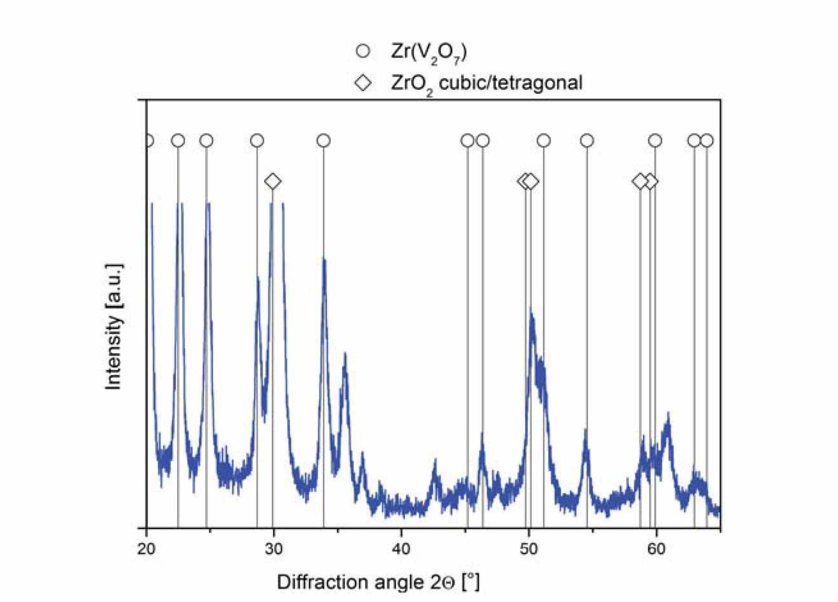

Fig. 4.23: XRD pattern showing peak positions of ZrV_2O_7 and cubic/tetragonal ZrO_2 after high temperature tribo testing of a ZrO_2 coating with 17.4 at% V at 600 °C in air.

According to the phase diagram ZrO_2-V_2O_5, it can be assumed the ZrV_2O_7 phase is stable at 600 °C and all of the available V in the coating is needed to form it. The excess of ZrO_2 remains cubic/tetragonal down to RT. The XRD peaks at about 36, 37, 38 and 42° cannot be identified by comparison with the ICDD powder diffraction files.

The ZrV_2O_7 phase is well described in literature. Withers et al. [46] discussed the phase transition of V_2O_5 and ZrO_2 into ZrV_2O_7 via in situ XRD. ZrV_2O_7 is structurally related to ZrW_2O_8 and known as a member of AM_2O_7 space groups which consist of a framework superstructure of corner connected AO_6 octahedra and VO_4 tetrahedra as shown in Fig. 4.24.

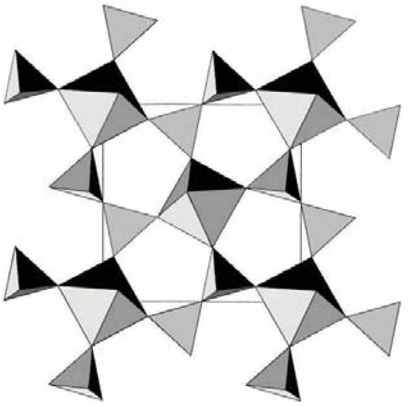

Fig. 4.24: Framework structure of the AM_2O_7 family adapted from [46].

There is scientific interest in the AM_2O_7 structure because of it's low isotropic negative thermal expansion coefficient between 100 °C and 800 °C [47]. Obviously this phase is formed at a temperature of 600 °C in air from the amorphous coating structure with 17.4 at% V synthesized at 150 °C.

The same results could be shown by Ge et al. for 50/50 mol% V_2O_5/ZrO_2 [48]. The binary equilibrium system of V_2O_5 and ZrO_2 (Fig. 4.25) shows this stoichiometric phase at about 50 mol% V_2O_5 in the zirconia matrix. The ZrV_2O_7 phase is stable up to 750 °C which agrees well with its formation during a tribological test at 600 °C (see Fig. 4.23).

Because no V-O compound like V_2O_5 can be detected with XRD measurements after high temperature tribological testing, Raman spectroscopy was conducted. V_2O_5 as well as VO_2 are Raman active, which means that the incident laser beam causes photon-phonon interactions in the material which can be detected as peaks (Raman shifts) at several wave numbers [cm^{-1}]. Only the sample with the highest V-content of 17.4 at% was investigated. The measured Raman curves are shown in Fig. 4.26 and compared to the those of V_2O_5 and VO_2 [38]. No consistency between the measured curves and these

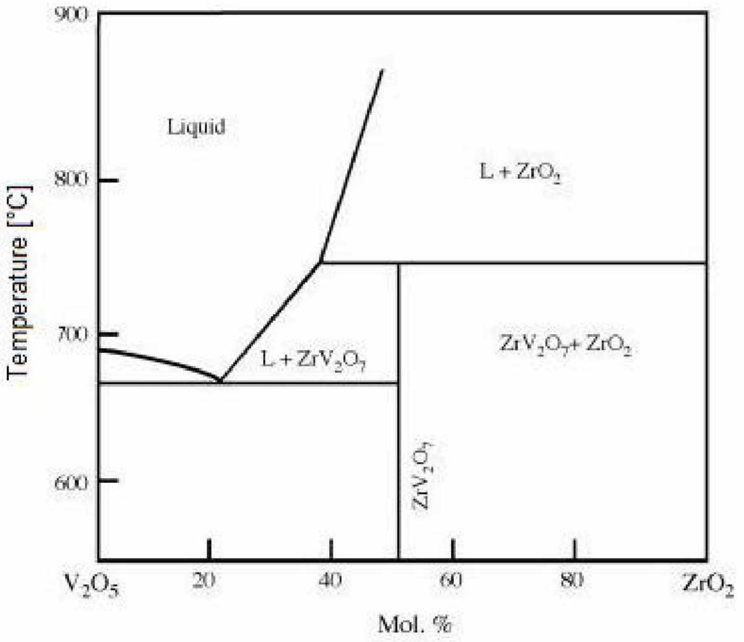

Fig. 4.25: Binary phase system of ZrO_2 and V_2O_5 showing the stoichiometric mixed phase ZrV_2O_7 adapted from [49].

standard curves can be seen. There seems to be no V_2O_5 or VO_2 in the coatings after annealing at 600 °C. However, peaks of ZrV_2O_7 at 780 and 990 cm^{-1} can definitely be shown as already found by XRD [50] [51].

The third temperature range for tribological tests was chosen at 800 °C because of an expected continuous formation of liquid V_2O_5 from the ZrV_2O_7 phase starting at temperatures above 750 °C according to the phase diagram in Fig. 4.25. Only the sample with a V content of 17.4 at% which shows a relatively good tribological performance at 600 °C without coating delamination was selected for tribological tests at 800 °C. The testing procedure is equal to that at 600 °C (2 N, 2000 laps). Indeed a low friction coefficient of 0.17 ± 0.02 can be demonstrated over the whole distance at 800 °C (see Fig. 4.27) without visible damage of the coating. That is as low as shown by Fateh et al. for VN coatings [52].

It was not possible to conduct optical white light profilometry testing for this sample after the tribological test because of the highly oxidized and rough surface. It seems likely that a liquid highly oxidized phase, which coalesces due to high surface tension, is formed. The wear track is identified as a shiny track with a polished look and a width of about 300 µm enclosed by oxidized surface (Fig. 4.28). Investigations of the wear track by a Nanofocus profilometer (Fig. 4.29) instead of optical white light profilometry show

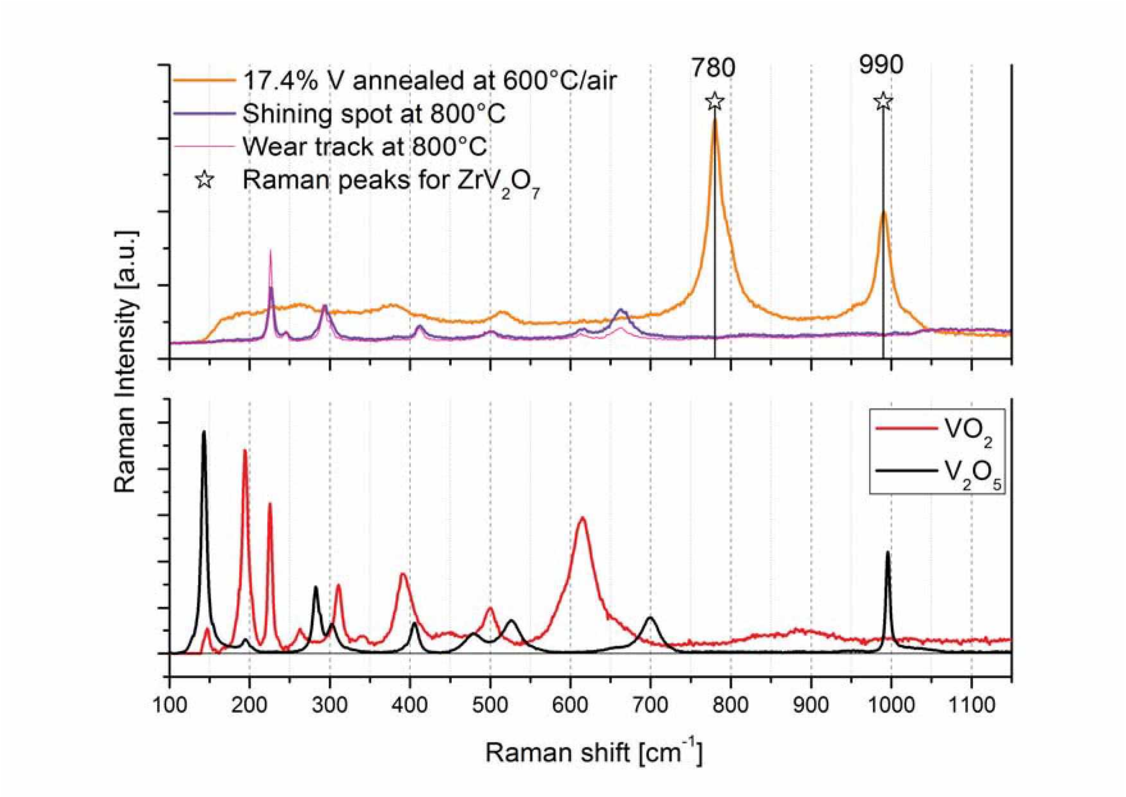

Fig. 4.26: Raman spectra of the V-containing ZrO_2 coatings after high temperature tribo testing at 600 °C and 800 °C compared to V_2O_5 and VO_2 standards [38].

a maximum exaltation of +40 µm instead of the usual shape of the wear tracks with negative profiles.

After high temperature tribological testing at 800 °C, XRD measurements were conducted again. The XRD pattern is shown in Fig. 4.30. The peaks can be indicated as monoclinic $(V_{0.05}Zr_{0.95})O_2$, monoclinic ZrO_2, V_2O_3 and Fe_2O_3. $V_{0.05}Zr_{0.95}O_2$ is a monoclinic stoichiometric mixed phase between V-O and Zr-O formed at elevated temperatures. Its existence might be a reason for the absent V_2O_5 because of further oxidation processes or valence reduction to V_2O_3. The analogous peak positions can be also attributed to Fe_2O_3 which may be caused by substrate oxidation. The XRD peaks at about 36, 37, 38 and 42° cannot be identified by comparing with the ICDD powder diffraction files.

The Raman spectra of the oxidized coating surface and of the wear track after high temperature tribological testing at 800 °C are shown in Fig. 4.26. Although there are clearly observable peaks compared to the as deposited sample, their positions do not correspond to V_2O_5 or VO_2. Furthermore, also for the shiny wear track at 800 °C with

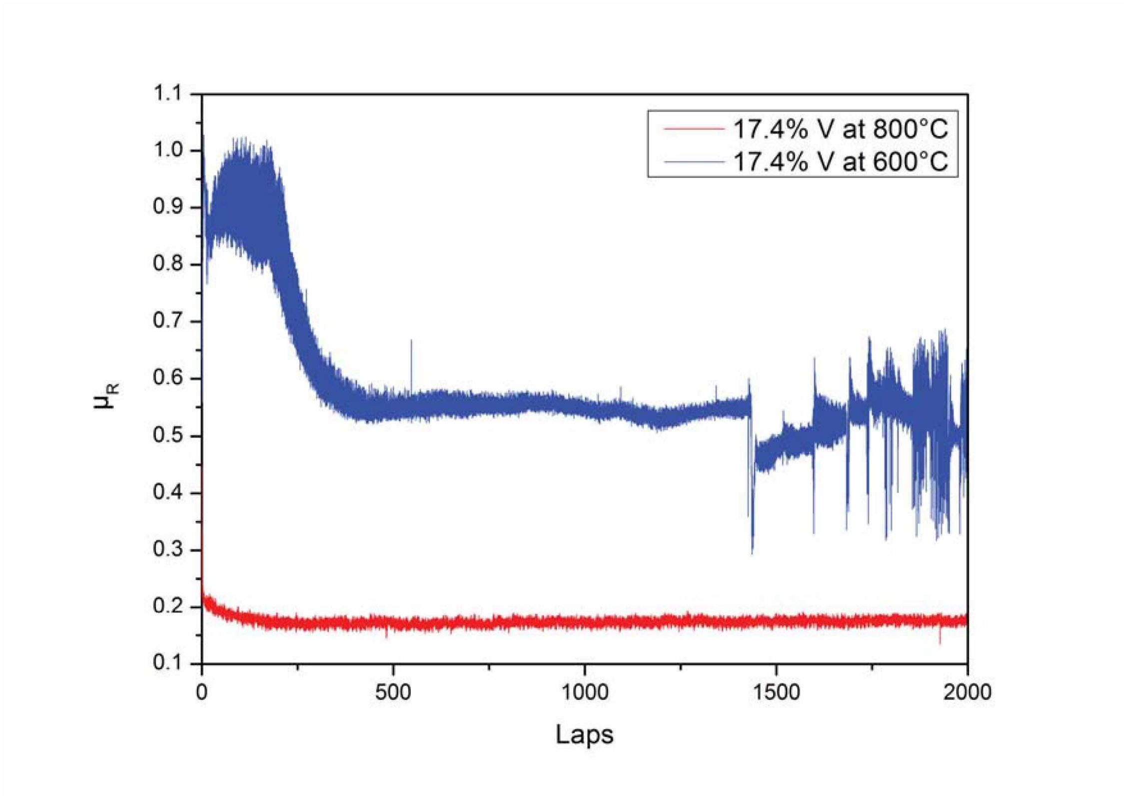

Fig. 4.27: Tribo-curves obtained at 800 °C compared to the one at 600 °C on the ZrO_2 coating with 17.4 at% V.

its very low friction coefficient of 0.17 no V-based Magnèli phases can be found by Raman.

4.3 Vacuum annealing

Additional Si-wafers are annealed in vacuum (pressure 10^{-6} mbar) to show possible differences in phase transformations and crystal structure. The annealing time is adapted to the one in air, to provide comparable growth conditions. The temperature of 700 °C is kept constant for 20 min. Fig. 4.31 shows that the XRD peaks after annealing at high temperatures in vacuum can be attributed to the cubic/tetragonal ZrO_2 phase instead of ZrV_2O_7 formed in air above 600 °C. This difference might be attributed to the different annealing atmosphere and/or the additional mechanical/thermal load in tribo testing.

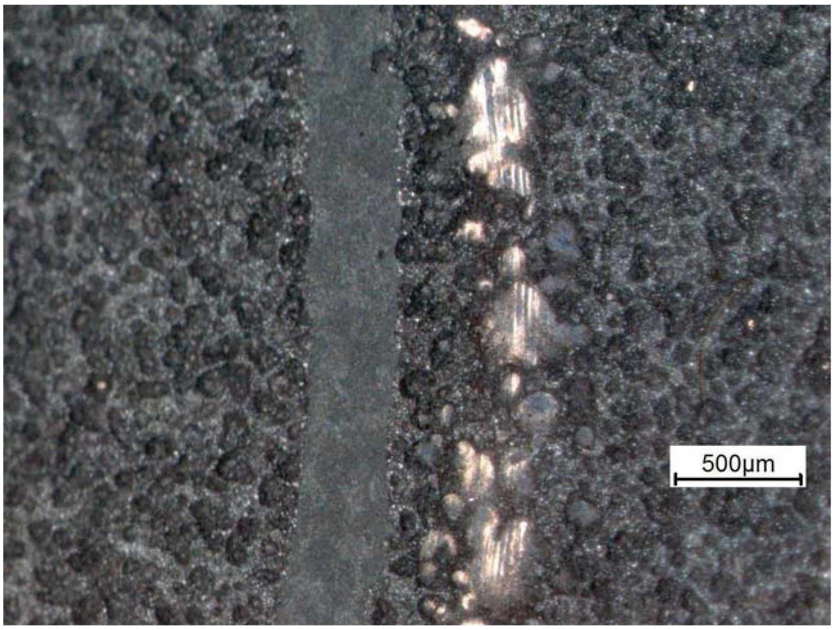

Fig. 4.28: Comparison of wear tracks on the ZrO_2 coating with 17.4 at% V after tribo testing at 600 °C (inner track) and 800 °C (outer track).

4.4 DSC Measurements

DSC measurements in synthetic air are conducted to gain further insights into the oxidation processes of the coatings. The measurements are evaluated in a qualitative way with respect to heat flow rates [mW/mg] and mass augmentation (thermal gravimetric measurements). The weights of the powders, which were evaluated with an accurate scale, were 24.1 mg with 2.2 at% V, 8.18 mg with 5.8 at% V and 33.64 mg with 17.4 at% V. The powders were put in small sintered Al_2O_3 cups because of possible melting phases which might react with platinum cups. In Fig. 4.32 the heat flow of all powders investigated are compared.

For all samples an increase of the heat flow occurs between 150 °C and about 350 °C which might probably be an oxidation reaction beyond the deposition temperature of 150 °C. From 400 °C to 1000 °C the curves show no even trend. There is one exothermic peak at about 620 °C and one endothermic peak at 770 °C for the coating with 17.4 at% V. For the samples with lower V-content (2.2 at%, 5.8 at%), the first DSC run shows a comparable trend with an exotermic peak at about 800 °C. Fateh et al. and Mayrhofer et al. reported on a similar trend for magnetron sputtered VN coatings showing a strong exothermic reaction due to oxidation between 500 and 800 °C during the first run and an endothermic peak at the melting point of V_2O_5 (670 °C) [52, 53].

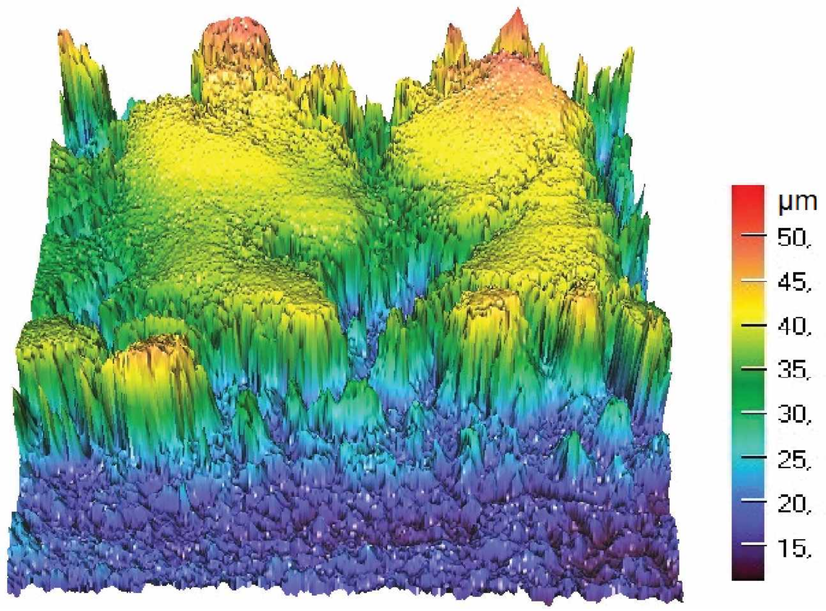

Fig. 4.29: Wear track of the ZrO_2 coating with 17.4 at% V at 800 °C investigated by Nanofocus measurements.

The thermal gravimetric analysis shows a continuous increase of the mass for all coating powders (see Fig. 4.33). The mass augmentations between RT and 1000 °C are about 4.5 % (for 2.2 at% V), 14.4 % (for 5.8 at% V) and 1.3 % for the sample with 17.4 at% V.

For all compositions, two reruns are carried out to investigate eventual reversible reactions or phase transformations. The reruns at lower V contents do not show unambiguous results. Just for the sample with 17.4 at% V, the reruns indicate a reversible reaction which can be assumed as endothermic (black dotted lines in Fig. 4.34) at about 660 °C which is very close to the melting temperature of V_2O_5 [52] [53] and a smaller endothermic peak at 800 °C which is attributed to the decomposition of ZrV_2O_7 into V_2O_5 and ZrO_2 [49].

Visually observing the Al_2O_3 cups after measurement, a yellow tarnish inside and outside is noticeable for all compositions (Fig. 4.35) after removing the powders.

To investigate if this yellow tarnish originates from absorbed liquid V-O compounds at high temperatures, the DSC cups were examined with Raman spectroscopy at two

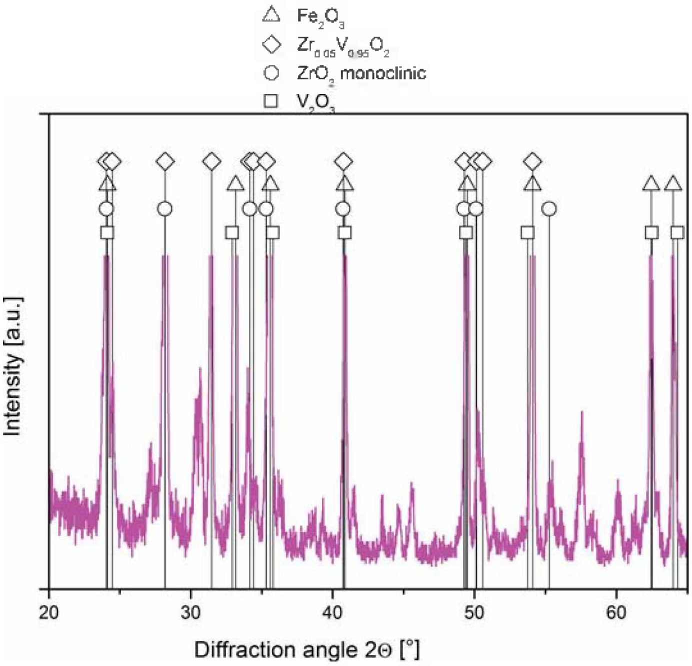

Fig. 4.30: XRD pattern of the ZrO_2 coating with a V content of 17.4 at% after high temperature tribo testing at 800 °C.

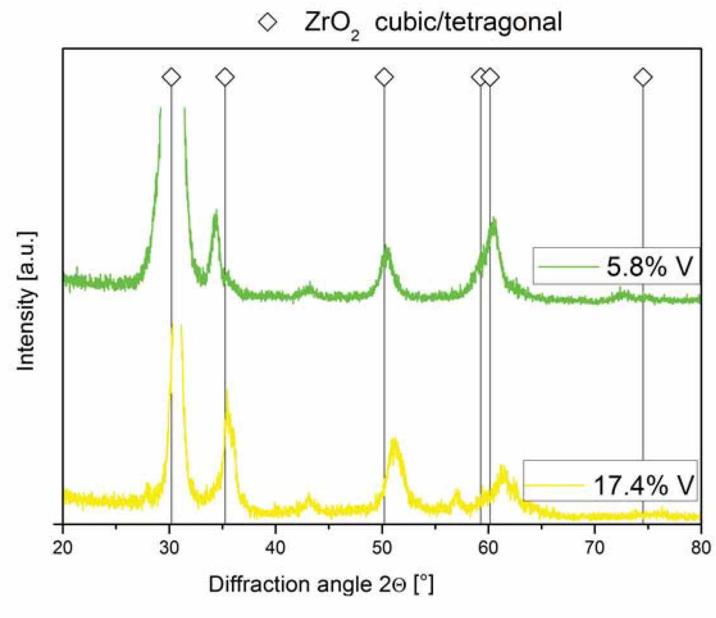

Fig. 4.31: Cubic/tetragonal ZrO_2 structure obtained after annealing of V-containing ZrO_2 coatings on Si wafers at 700 °C in vacuum.

different positions: first, a point is aimed which is not yellow coloured to create a reference for the sintered Al_2O_3 which is also Raman active. In a second step, the bottom

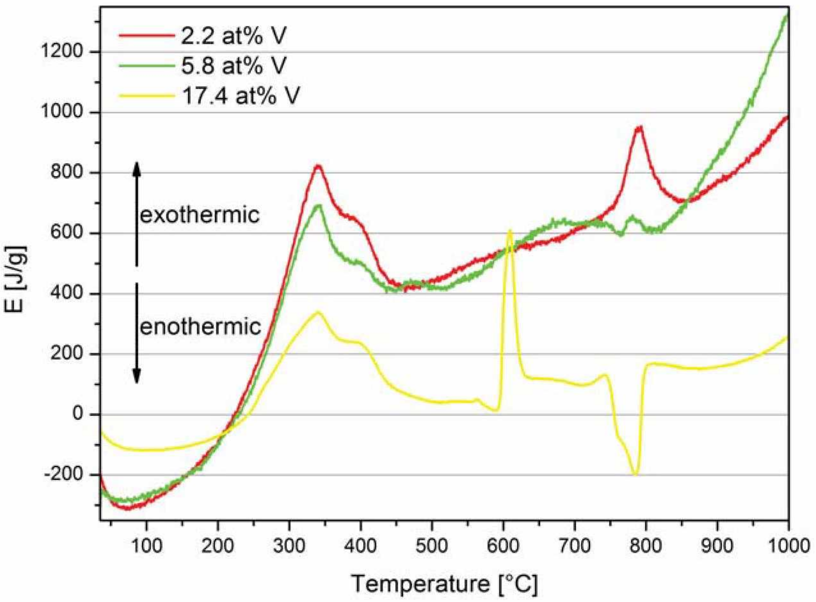

Fig. 4.32: DSC runs of all V-doped ZrO_2 powders from RT up to 1000 °C in synthetic air.

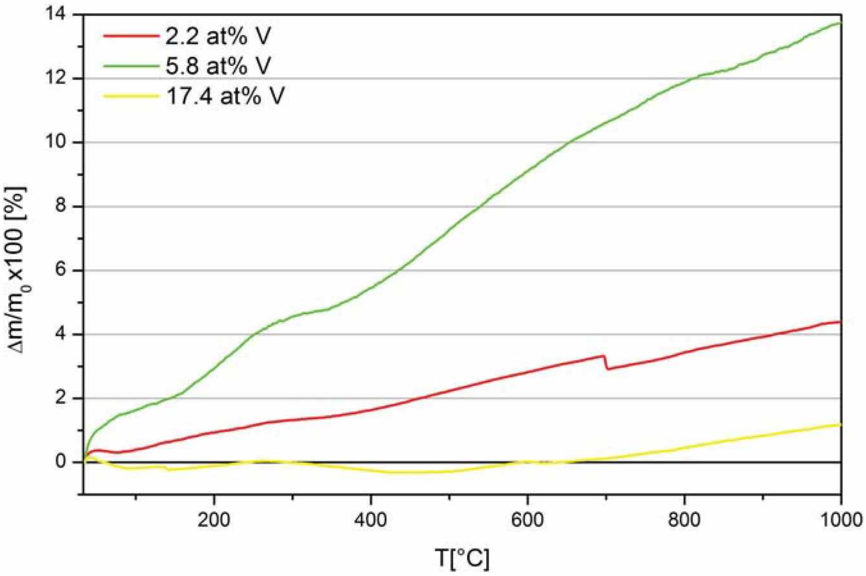

Fig. 4.33: Change of mass of the V-containing ZrO_2 powders during DSC measurements in synthetic air.

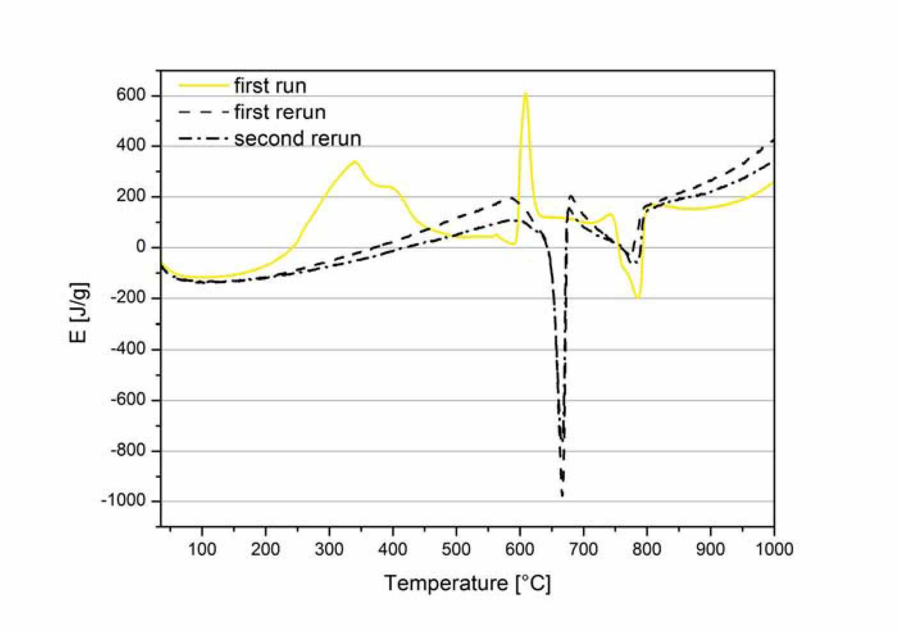

Fig. 4.34: DSC run of the sample with 17.4 at% V compared with it's first and second rerun showing an endothermic reaction at about 660 °C.

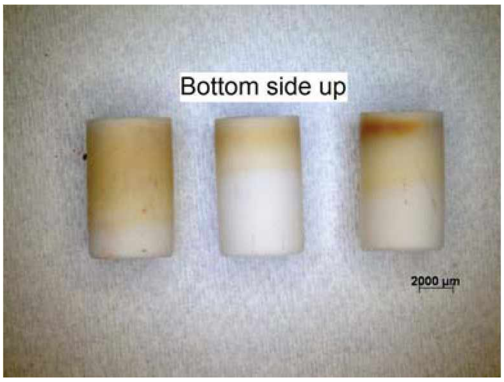

Fig. 4.35: Sintered Al_2O_3 DSC cups after measurements up to 1000 °C with yellow tarnish (17.4 at% V left, 2.2 at% V middle, 5.8 at% V right).

side of the cup is measured focusing on the yellow tarnish. As shown in Fig. 4.36, the V_2O_5 standard fits perfectly to the pattern obtained for the bottom side of the cup [38]. It can be concluded that the yellow colour on the cups is due to absorption of molten V_2O_5 by the porous sintered cups. Thus, in the first run for the sample with 17.4 at% V ZrV_2O_7 is formed, indicated by the exothermic DSC peak at about 620 °C (see Fig. 4.34). Then V_2O_5 precipitates and melts (peak at 770 °C, compare Fig. 4.25). The molten V_2O_5 infiltrates the porouos sintered cups but does not react again upon cooling. The endothermic peaks of the reruns indicate the repeated melting of V_2O_5 at

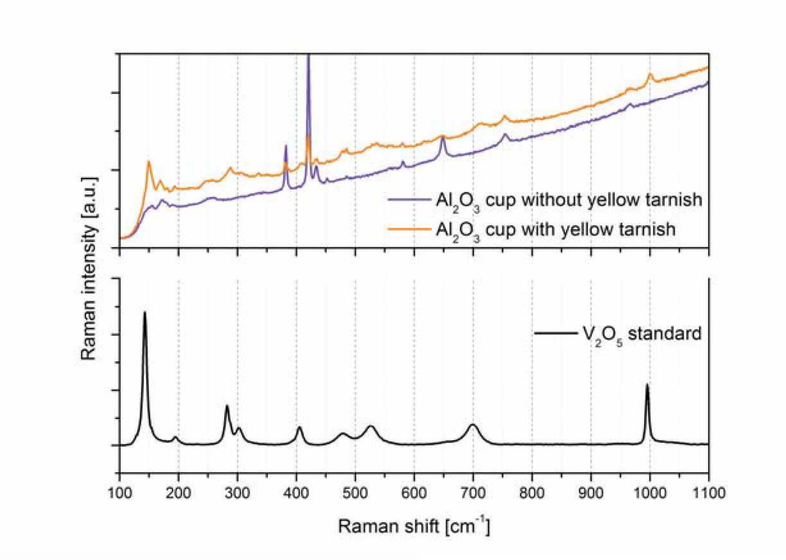

Fig. 4.36: Raman spectra of the yellow coloured Al_2O_3 cup after DSC measurements of the ZrO_2 powder containing 17.4 at% V up to 1000 °C in air and reference spectra for V_2O_5 and VO_2 [38].

660 °C.

In summary, the DSC measurements show that it possible to obtain self-lubricious and thermal management effects with the deposited coatings in the temperature range between 600 and 800 °C where the endothermic reaction at 660 °C could contribute to a reduction of local flash temperatures in severe sliding contacts.

5 Summary and Conclusions

Within the scope of this thesis, the influence of V on reactively magnetron sputtered non stabilized zirconia coatings is investigated with respect to its structural and mechanical properties as well as its thermal management abilities for high temperature sliding interfaces.

Three types of V-doped ZrO_2 coatings with different V-contents of 2.2, 5.8 and 17.4 at% have been synthesized at 150 °C by a reactive unbalanced magnetron sputtering device on Si (100), M2 steel and Fe-substrates. The tribological performance of these coatings is compared to undoped ZrO_2 thin films in a temperature range between RT and 800 °C.

The achieved coating thicknesses after 240-360 min deposition time are between 1.2 and 2.3 µm with constant surface roughness values for all compositions of about 10 ± 2 nm. The XRD pattern of the as deposited coatings show a change of the crystal structure of the zirconia matrix with increasing V-content from monoclinic (undoped, 2.2 at% V) to cubic (5.8 at% V) and an X-ray amorphous structure (17.4 at% V), independent of the substrates.

Compared to other coating systems, the maximum stresses are quite low in a range of -400 and 150 MPa. The hardness of the coatings decreases from 17 GPa (constant for V-contents up to 5.8 at%) to 7.4 GPa at 17.4 at%. The Young's modulus values display a similar trend as the hardness, decreasing from a value of 220-240 GPa (up to a V content of 2.2 at%) to 152 GPa for the amorphous coating. The tribological measurements at RT indicate friction coefficients of 0.2 and below for the undoped zirconia coating and the one with low V-content of 2.2 at% sliding against alumina balls. The higher the V-contents, the higher is the friction coefficient and the broader are the wear tracks. During tribological testing at 600 °C, friction coefficients between 0.4 and 0.8 are measured within the first laps followed by coating delamination. After tribological tests at 600 °C, the stoichiometric mixed phase ZrV_2O_7 is detected by XRD. This phase is stable up to 750 °C and prevents segregation of V_2O_5, and thus no self-lubrication occurs. The formation of ZrV_2O_7 is fostered by DSC measurements showing an exothermic peak at

620 °C. A low friction coefficient of 0.17 is detected at 800 °C for a V-content of 17.4 at%. There, the monoclinic zirconia phase can be assumed to be the mechanically stable phase. By DSC measurements, a strongly endothermic reaction can be detected at about 670 °C (i.e. at the melting point of V_2O_5). An additional small endothermic reaction originates from precipitation of V_2O_5 out of ZrV_2O_7 which is assumed to be responsible for the observed low friction coefficient.

In summary, it can be concluded that it is possible to achieve self lubricating behavior in zirconia based coatings with sufficiently high V-contents at temperatures of 800 °C, where the lubricating V_2O_5 is formed by an endothermic reaction. This reaction might provide thermal management abilities, by reducing local flash temperatures occuring in sliding contacts.

6 Outlook

Ultimately, an outlook on possible further procedures to improve the investigated complex coating system of vanadium oxides in a zirconia matrix may be given.

1. For the coating with 17.4 at% V that showed low friction behaviour at 800 °C, the composition of the sliding film should be investigated to understand the underlying low friction mechanisms.

2. More detailed Raman investigations could help to detect possible small amounts of ternary Zr-V-O phases that could not be identified yet.

3. Additional to DSC investigations, in situ XRD measurements may help to study the phase transformations at high temperatures.

4. The adhesion between the coatings and the M2 substrates may be improved by an interlayer.

5. Furthermore, a multilayer arrangement has to be considered, containing diffusion barrier layers to control out-diffusion of the formed V_2O_5.

List of Figures

Bibliography

[1] A. A. Voevodin, D. V. Shtansky, E. A. Levashov, and J. J. Moore. *Nanostructured Thin Films and Nanodispersion Strengthened Coatings*. Kluwer Academic Publishers, Dordrecht, 2003.

[2] C. Muratore, J. J. Hu, and A. A. Voevodin. Tribological coatings for lubrication over multiple thermal cycles. *Surface and Coatings Technology*, 203:957 – 962, 2009.

[3] A. A. Voevodin, T. A. Fitz, J. J. Hu, and J. S. Zabinski. Nanocomposite tribological coatings with "chameleon" surface adaptation. *Journal of Vacuum Science and Technology A: Vacuum, Surfaces and Films*, 20:1434–1444, 2002.

[4] J. J. Hu, C. Muratore, and A. A. Voevodin. Silver diffusion and high-temperature lubrication mechanisms of YSZ-Ag-Mo based nanocomposite coatings. *Composites Science and Technology*, 67:336–347, 2007.

[5] K. Koski, J. Hölsä, and P. Juliet. Properties of zirconium oxide thin films deposited by pulsed reactive magnetron sputtering. *Surface and Coatings Technology*, 120-121:303 – 312, 1999.

[6] J. D. McCullough and K. N. Trueblood. The crystal structure of baddeleyite (monoclinic ZrO_2). *Acta Cryst.*, 12:507–511, 1959.

[7] H. A. Wriedt and T. B. Massalski. *Binary Alloy Phase Diagrams*. ASM International, Materials Park Ohio, 1990, 2nd edition.

[8] http://commons.wikimedia.org/wiki/file:kristallstruktur_zirconium.

[9] N. Fateh, G. Fontalvo, and C. Mitterer. Structural and mechanical properties of dc and pulsed dc reactive magnetron sputtered V_2O_5 films. *Journal of Physics D: Applied Physics*, 40:7716–7719, 2007.

[10] P. Balog, D. Orosel, Z. Cancarevic, S. Schön, and M. Jansen. V_2O_5 phase diagram revisited at high pressures and high temperatures. *Journal of Alloys and Compounds*, 429:87–98, 2007.

[11] http://en.wikipedia.org/wiki/V2O5.

[12] J. Galy, A. Ratuszna, J. Iglesias, and A. Castro. Complex thermal evolution of V_2O_5 and MO_3 cell parameters in the range $15 < T [K] < 900$. Solid State Sci. 8:1438–1442, 2006.

[13] Y. Ningyi, L. Jinhua, and L. Chenglu. Valence reduction process from sol-gel V_2O_5 to VO_2 thin films. *Applied Surface Science*, 191:176–180, 2001.

[14] N. Fateh. *Low-friction Coatings Based on Lubricious Vanadium Oxides*. PhD thesis, Montanuniversität Leoben, Austria, 2008.

[15] A. Erdemir. Transfer of 319 Al alloy to titanium diboride and titianium nitride base coatings: efects of sliding speed, temperature and environment. *Surface and Coatings Technology*, 200:2260–2270, 2005.

[16] M. Ohring. *Materials Science of Thin Films*. Academic Press, New York, 2002, 2nd edition.

[17] W. D. Westwood. *Sputter Deposition*. Wiley, New York, 2003.

[18] F.W. Bach, A.L. Laarmann, and T. Wenz. *Modern Surface Technology*. Wiley-VCH, Weinheim, 2006.

[19] M. V. Ramana Murty. Sputtering: the material erosion tool. *Surface Science*, 500:523 – 544, 2002.

[20] P. H. Mayrhofer. *Materials Science Aspects of Nanocrystalline PVD Hard Coatings*. PhD thesis, Montanuniversität Leoben, 2001.

[21] M. S. Wong, W. J. Chia, P. Yashar, J. M. Schneider, W. D. Sproul, and S. A. Barnett. High-rate reactive d.c. magnetron sputtering of ZrO_2 coatings. *Surface and Coatings Technology*, 86-87:381 – 387, 1996.

[22] J. A. Theil, E. Kusano, and A. Rockett. Vanadium reactive magnetron sputtering in mixed Ar/O_2 discharges. *Thin Solid Films*, 298:122 – 129, 1997.

[23] *Advanced Technical Ceramics - Methods of test for ceramic coatings.* Deutsches Institut für Normung e.V. DIN EN 1071, Berlin.

[24] K. Nitzsche. *Schichtmesstechnik.* Vogel, Würzburg, 1996.

[25] H. Jehn. *Charakterisierung dünner Schichten.* Beuth Verlag, Berlin, 1993.

[26] ICDD at http://www.icdd.com.

[27] D. Winkler. Konzeption und Realisierung eines thermisch unterstützten Messverfahrens zur Bestimmung von Eigenspannungen in dünnen Schichten. Master's thesis, Montanuniversität Leoben, 1997.

[28] L. B. Freund and S. Suresh. *Thin Film Materials.* Cambridge University Press, Cambridge, 2003.

[29] A. C. Fischer-Cripps. *Nanoindentation.* Springer, New York, 2nd Edition, 2004.

[30] D. Reitberger. Beschichtung von Werkzeugen für den Kunststoff-Spritzguss. Master's thesis, Montanuniversität Leoben, 2001.

[31] E. Rabinowicz. *Friction and Wear of Materials.* John Wiley Inc., New York, 2nd edition, 1995.

[32] I. Hutchings. *Tribology - Friction and Wear of Engineering Materials.* Edward Arnold, London, 1992.

[33] *Wyko NT1000 Operators Guide.*

[34] *Wyko Surface Profilers, Technical Reference Manual.*

[35] http://en.wikipedia.org/wiki/raman_spectroscopy.

[36] R. L. McCreery. *Raman Spectroscopy for Chemical Analysis.* Wiley-Interscience, Weinheim, 2000.

[37] N. Fateh, G.A. Fontalvo, L. Cha, T. Klünsner, G. Hlawacek, C. Teichert, and C. Mitterer. Synthesis-structure relations for reactive magnetron sputtered V_2O_5 films. *Surface and Coatings Technology*, 202:1551 – 1555, 2008.

[38] R. Franz. *AlCrVN - Design of High-temperature Low-friction Coatings.* PhD thesis, Montanuniversität Leoben, 2007.

[39] S. Kouteva-Arguirova, W. Seifert, M. Kittler, and J. Reif. Raman measurement of stress distribution in multicrystalline silicon materials. *Materials Science and Engineering B*, 102:37 – 42, 2003.

[40] http://www.fh-muenster.de/maschinenbau/downloads/werkstofftechnik.

[41] K. Holmberg and A. Matthews. *Coatings Tribology.* Elsevier, Amsterdam, 1994.

[42] S. Graça, R. Colaço, A. J. Kulik, and R. Vilar. A displacement sensing nanoindentation study of tribo-mechanical properties of the Ni-Co system. *Applied Surface Science*, 254:7306 – 7313, 2008.

[43] R. N. Patil and E. C. Subbarao. Axial thermal expansion of ZrO_2 and HfO_2 in the range room temperature to 1400°C. *Journal of Applied Crystallography*, 2:281–288, 1969.

[44] http://www.novawafers.com/resources-about-silicon.html.

[45] S. Grasser. Influence of Pulsed Bias on CrN Coatings Prepared by Reactive Magnetron Sputtering. Master's thesis, Montanuniversität Leoben, 2008.

[46] R. L. Withers, J. S. Evans, J. Hanson, and A. W. Sleight. An in situ temperature-dependent electron and x-ray diffraction study of structural phase transitions in ZrV_2O_7. *Journal of Solid State Chemistry*, 137:161 – 167, 1998.

[47] J. Evans, J.C. Hanson, and A.W. Sleight. Room-temperature superstructure of ZrV_2O_7. *Acta Crystallographica Section B: Structural Science*, 54:705–713, 1998.

[48] J. Ge, M. Xue, Q. Sun, A. Auroux, and J. Shen. Surface acidic and redox properties of V-Zr-O catalysts for the selective oxidation of toluene to benzaldehyde. *Journal of Molecular Catalysis A: Chemical*, 278:209 – 214, 2007.

[49] H. M. Ondik and H. F. McMurdie. *Phase Diagrams for Zirconium and Zirconium Systems.* Wiley Interscience, Weinheim, 1998.

[50] D. Gazzoli, S. D. Rossi, G. Ferraris, G. Mattei, R. Spinicci, and M. Valigi. Bulk and surface structures of V_2O_5/ZrO_2 catalysts for n-butane oxidative dehydrogenation. *Journal of Molecular Catalysis A: Chemical*, 310:17 – 23, 2009.

[51] D. Gazzoli, S. D. Rossi, G. Ferraris, M. Valigi, L. Ferrari, and S. Selci. Morphological and textural characterization of vanadium oxide supported on zirconia by ionic exchange. *Applied Surface Science*, 255:2012 – 2019, 2008.

[52] N. Fateh, G.A. Fontalvo, G. Gassner, and C. Mitterer. Influence of high-temperature oxide formation on the tribological behaviour of TiN and VN coatings. *Wear*, 262:1152 – 1158, 2007.

[53] P. H. Mayrhofer, P. Eh. Hovsepian, C. Mitterer, and W. D. Münz. Calorimetric evidence for frictional self-adaptation of TiAlN/VN superlattice coatings. *Surface and Coatings Technology*, 177-178:341 – 347, 2004.